*Article*

# Elimination of Indoor Volatile Organic Compounds on Au/SBA-15 Catalysts: Insights into the Nature, Size, and Dispersion of the Active Sites and Reaction Mechanism

Emmanuel Iro [1], Hiroko Ariga-Miwa [2], Takehiko Sasaki [3], Kiyotaka Asakura [2] and Maria Olea [1,*]

[1] School of Science, Engineering and Design, Teesside University, Middlesbrough TS1 3BX, UK
[2] Institute of Catalysis, Hokkaido University, Sapporo 001-0021, Japan
[3] Graduate School of Frontier Sciences, The University of Tokyo, Kashiwanoha 277-8561, Japan
[*] Correspondence: mo506@cam.ac.uk

**Abstract:** Gold catalysts, with different particle sizes ranging from 19 to 556 Å, and supported on SBA-15 mesoporous silica, were prepared by using deposition-precipitation, co-precipitation, and impregnation methods. All samples were characterised by TEM, EXAFS, XPS, XRD, CFR (Continuous Flow Reactor), and TPR. The sample which proved to have the highest activity was characterised by TAP (Temporal Analysis of Products) as well. XPS, wide-angle XRD, EXAFS, and $H_2$-TPR measurements and data analysis confirmed that gold was present as $Au^0$ only on all samples. The size of the Au nanoparticle was determined from TEM measurements and confirmed through wide-angle XRD measurements. EXAFS measurements showed that as the Au-Au coordination number decreased the Au-Au bond length decreased. TEM data analysis revealed a dispersion range from 58% (for the smallest particle size) to 2% (for the highest particle size). For Au particles' sized lower that 60 Å, the Au dispersion was determined using a literature correlation between the dispersion and EXAFS Au-Au coordination number, and was in good agreement with the dispersion data obtained from TEM. The Au dispersion decreased as the particle size increased. CFR experiments validated the relationship between the size of the gold particles in a sample and the sample's catalytic activity towards acetone oxidation. The lowest temperature for the acetone 100% conversion, i.e., 250 °C, was observed over the reduced catalyst sample with the smallest particle size. This sample not only showed the highest catalytic activity towards acetone conversion, but, at the same time, showed high reaction stability, as catalyst lifetime tests, performed for 25 h in a CFR at 270 °C for the as-synthesised sample, and at 220 °C for the reduced sample, have confirmed. TAP (Temporal Analysis of Products) measurements and data analysis confirmed a weak competitive adsorption of acetone and oxygen over the Au/SBA-15 sample. Based on TAP data, a combination of Eley–Rideal and Langmuir–Hinshelwood mechanisms for acetone complete oxidation was proposed.

**Keywords:** gold catalysts; SBA-15 support; VOCs; active sites; reaction mechanism

## 1. Introduction

People living in cities spend up to ninety percent of their time indoors unaware that indoor air pollution levels often exceed those of outdoors. Many of the pollutants cause symptoms which may not occur for many years, and as such, make it difficult to discover the cause. Asthma, other breathing disorders, and even cancer are examples of potentially serious effects caused by exposure to indoor air pollutants [1]. Volatile organic compounds (VOCs) are the major components in air pollutants. VOCs are organic compounds with boiling points in the range of 50–260 °C at room temperature and atmospheric pressure of 133 Pa. There is a growing concern to monitor and efficiently eliminate harmful volatile organic compounds emitted by the many new building materials, furnishings, printers, pressed wood, wood stoves, and household products in indoor spaces. For example, there is a series of harmful chemical substances, such as VOCs, present in indoor air following

the use of air freshers. The air fresheners category includes incenses, natural products, scented candles, and aerosols, to name a few [1]. Eggert and Hansen measured total VOCs emission from one stick or cone of incense, which "varied between 6 and 121 mg [2]. If those amounts were evenly distributed in a 20 m$^3$ room without ventilation it would result in 300 to 6000 μg/m$^3$" [1]. Similar results were obtained by Manoukian et al. [3].

There are a variety of approaches for controlling VOCs in indoor environments such as source control, ventilation, and air cleaning. At present, air purification remains one of the most promising air-cleaning methods that involves diverse control techniques, e.g., adsorption by activated carbon, photocatalytic oxidation, biological treatment, catalytic oxidation, absorption, and ionization methods, to mention a few [4–6].

Among the technologies available to clean-up indoor VOCs, the total oxidation to less harmful compounds ($CO_2$, $H_2O$, and HCl) by heterogeneous catalysis offers the best potential to eliminate VOCs even at very low concentrations, i.e., parts per billion (ppb) levels, peculiar to indoor air. What is more, catalytic oxidation technology is regarded as an efficient method because of its effectiveness against low levels of the generation of secondary pollutants and possibility to control the selectivity of the by-products [7]. The main challenge is the development of active and stable catalysts that can operate at temperatures as low as ambient temperatures, in order to reduce the high costs of running indoor catalytic air clean-up systems and avoid the formation of unwanted by-products such as NOx produced by high temperature oxidation reactions. Since VOCs are stable organic compounds, it is extremely difficult to carry out the total catalytic oxidation of most of them below 200 °C.

Selection of the catalytic materials for various organic pollutants is a very challenging task, due to the large variety of VOCs and the complex nature of VOCs mixtures [8]. Catalysts used for complete oxidation of VOCs are classified into three main groups: noble metal-based catalysts, transition metal oxide catalysts, and alloy catalysts [9]. Regarding metal oxide catalysts, in particular Co, Mn, Cu, Ni, Mo, and V oxides, although they show significant activity and are cheap, they are not sufficiently stable [10]. However, increased stability was shown by CuxCeMgAlO mixed oxide catalysts derived from multicationic LDH (Layered Double Hydroxide) precursors for methane total oxidation [11]. Though noble metal catalysts are expensive, they are still largely preferred because they show lower light off temperatures in complete oxidation of VOCs. Their catalytic activity depends on the noble metal and varies with the nature of VOC [12]. Mostly studied so far are Pt or Pd or both, supported on γ-$Al_2O_3$ or $CeO_2$–$Al_2O_3$ mixed oxides [13]. However, the most noble of all, Au in bulk form, was for a long time the exception. It was not until the unprecedented discovery by Haruta [14,15] that supported gold nanoparticle (1–5 nm) catalysts exhibited the lowest temperature CO total oxidation, i.e., −77 °C, compared to any other catalyst, which suggested that gold could possibly be the answer for low temperature total oxidation of VOCs as well. More than 30 years on, although there is an agreement on the high catalytic activity of gold nanoparticles, there is still a scientific debate encompassing the nature of the active sites. Despite extensive research, no unambiguous identification of the active site's nature in CO oxidation has been reported to date [16–19]. However, it has been reported that the activity of gold-based catalysts depends on the size of the gold nanoparticles on the support (the smaller the gold, the more active the catalyst), on the degree of dispersion of gold onto support, on gold–support interaction, on oxidation state (s) of gold, and on the nature of the catalyst support [20–23].

Typically, the active phases are deposited on a suitable support. Several types of supports with good thermal stability and high surface area have been used, such as, $Al_2O_3$, $ZrO_2$, $CeO_2$, $SiO_2$, $TiO_2$, $SnO_2$, CuO, $Fe_2O_3$, $La_2O_3$, MgO, montmorillonite, zeolites, and carbon-based materials. The use of nanotubular materials as catalyst supports, in which the active centres are nanoparticles inside the tubes, has also been investigated. Carbon nanotubes, boron nitride nanotubes, and halloysite nanotubes are some typical examples of the nanotubular supports reported [6].

Among them, SBA-15 mesoporous silica has the potential to become an excellent support for gold nanoparticles as it offers a very high surface area for gold dispersion, with ordered mesopores large enough to accommodate gold nanoparticles in its internal and external surfaces, as well as allowing easy access of reactant molecules to the active sites. In addition, SBA-15 has high structural, thermal, and hydrothermal stability [24–26].

As for the VOCs total oxidation on supported gold nanoparticles, the literature data is scarce and even scarcer for VOCs oxidation on Au/SBA-15 [27]. The few examples are as follows: Walters et al. [28] reported the high activity of $Au/Co_3O_4$ for the combustion of methane, whereas Haruta et al. [29] reported the high activity of $Au/\alpha Fe_2O_3$ for the combustion of methanol, formaldehyde, and formic acid. A recently published review by Kim et al. [30] deals with trends for VOC removal on noble-metal-based catalysts. Ag, Au, Pd, Pt, and Pd-Ce catalysts supported on different supports were considered for the total oxidation of toluene, benzene, xylene, and cyclooctane, respectively, focusing mainly on the mechanism and kinetics. However, the most recent review on acetone catalytic removal [31] lists manganese-based catalysts as the more used ones, followed by cerium-based, cobalt-based, platinum-based, and palladium-based ones. There is no mention of gold-based catalysts at all.

Minicò et al. [32] studied the complete oxidation of 2-propanol, ethanol, methanol, acetone, and toluene over an Au/iron oxide. As for acetone, the complete conversion was observed at around 300 °C. Scirè et al. [33] studied the complete methanol, acetone, and toluene oxidation over an $Au/CeO_2$ catalyst. The temperature required for the complete oxidation of acetone was around 300 °C and slightly varied with the preparation method of the catalysts, i.e., deposition precipitation or coprecipitation.

Au/oxide catalysts, where is the oxides are MgO, $Y_2O_3$, CuO and NiO, were used to study the total oxidation of acetyl acetate and toluene. As such, the relationship between catalytic activity and the support reducibility was established [34].

To the best of our knowledge, there is no published data on developed Au/SBA-15 catalysts tested for VOCs oxidation.

Therefore, the aim of this study is to undoubtedly clarify the nature of gold active sites, to determine their size and dispersion, and also to give insights into the VOCs total oxidation mechanism using acetone as the model molecule over the in-house designed and prepared Au/SBA-15 catalyst's samples. Acetone was chosen as the model molecule because it is one of the most abundant oxygen-containing VOCs in the atmosphere, and it is also one of the most widely present indoor VOCs species [31].

## 2. Results and Discussion

The nature of the gold species on SBA-15 was investigated through XPS and TPR measurements and data analysis. The oxidation state of gold was undoubtedly assessed by means of X-ray photoelectron spectroscopy. As seen in Figure 1, all fresh samples show Au ($4f_{7/2}$) BE values at 84.3 $\pm$ 0.3 eV and FWHM in the range of 1.8–2.3 eV. As for the spent samples, Au-en/SBA-15 and Au-0.6Mdp/SBA-15 show similar features as the fresh ones, with Au ($4f_{7/2}$) BE values at 84.1 and 83.8 eV and FWHM of 2.1 and 1.8 eV, respectively. The spent Au-P/SBA-15 sample shows a rather different feature. Another clearly resolved Au $4f_{7/2,5/2}$ doublet is observed on the lower binding energy side, which can be attributed to two chemically Au environments [35]. In other words, Au clusters in different positions have different charge effects to make the shift. This finding is supported by the TEM images, which show that there are gold nanoparticles grown on the surface (Au-Silica environment) of the support along with gold nanoparticles grown on top of each other (Au-Au environment).
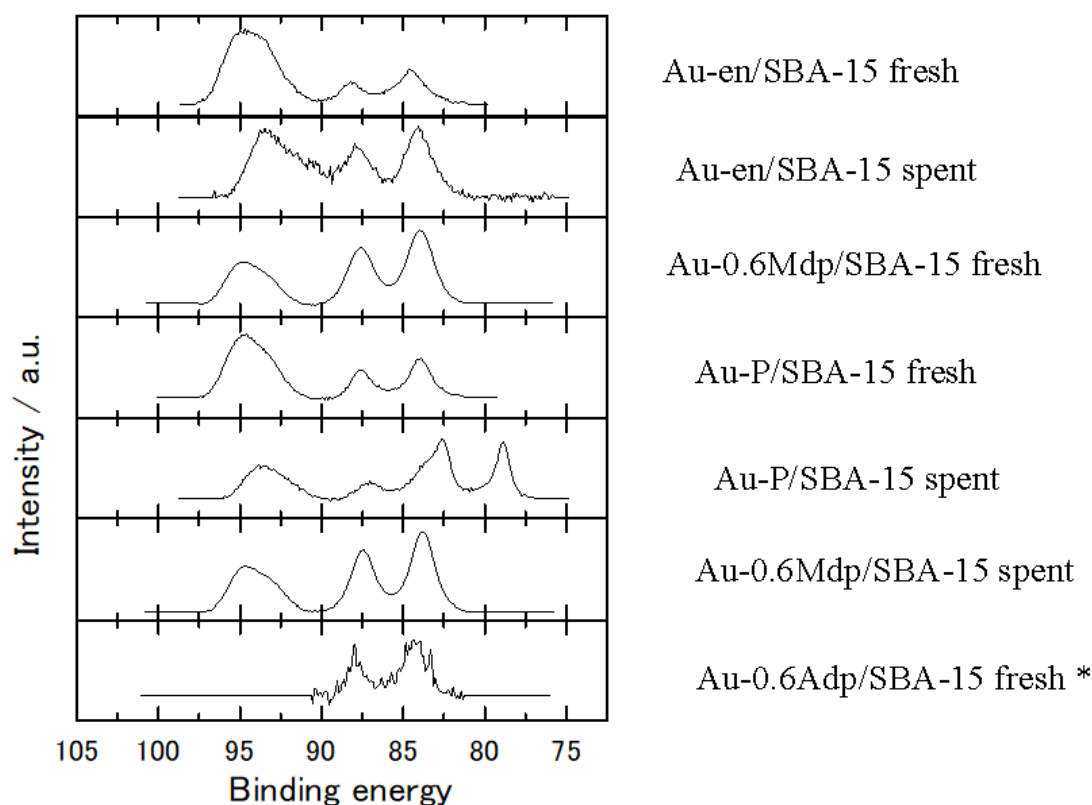
**Figure 1.** XPS spectra in the Au (4f) region for all tested samples. (* The measurement was limited to the 82–91 eV region; because of low count, it would have taken too long time to measure the extended region).

Compared to the Au (4f) region recorded on Au foil which showed an Au ($4f_{7/2}$) BE value of 84.0 eV and FWHM of 1.8 eV, three of the four as-made samples, namely Au-en/SBA-15, Au-0.6Mdp/SBA-15 and Au-0.6Adp/SBA-15, show a slightly broader feature; the full width at half maximum was 2.3 eV for the first one and 2.0 eV for the last two. In accordance with the literature, peak broadening could be attributed either to a differential charging effect arising from the insulating nature of the support suggesting the presence of gold species with inhomogeneous cluster size distribution [36] or to different oxidation state [32]. The peak broadening is most probably due to the presence of gold clusters with different sizes. TEM measurements support this statement, as seen below. The Au-P/SBA-15 spent catalyst shows abnormal XPS spectra; two pairs of Au peaks with further lower energy are discussed below.

Table 1 presents the XPS features of all samples.

For all samples except the Au-P/SBA-15 spent one, the peaks of Au ($4f_{5/2}$) and Au ($4f_{7/2}$) are centered at 87.7 ± 0.4 eV and 84.2 ± 0.4 eV, respectively, indicating the presence of gold in the metallic state. These results are in good agreement with the literature. It was found that gold is present just as $Au^0$ at calcination temperatures higher than 300 °C [32]. For all our samples, the calcination temperature was 500 °C.

The peak appearing between 90 and 96 eV for all samples but the Au-0.6Adp/SBA-15 fresh one was assigned to Si (2p), which was excited by Mg $K\alpha_{3,4}$.

As seen in Figure 1, the Au (4f) peaks for the Au-0.6Adp/SBA-15 fresh sample are weaker than that of all other measured samples since its Au/Si surface ratio is the lowest one among the samples studied.

**Table 1.** XPS features of all samples.

| Sample | Au(4f$_{7/2}$) (eV) | Au(4f$_{5/2}$) (eV) | Peak Distance (eV) | FWHM Au(4f$_{7/2}$) (eV) | Au/Si Ratio (Surface) |
|---|---|---|---|---|---|
| Au-en/SBA-15 fresh | 84.6 | 88.1 | 3.5 | 2.3 | 0.0031 |
| Au-en/SBA-15 spent | 84.1 | 87.7 | 3.6 | 2.1 | 0.0051 |
| Au-0.6Mdp/SBA-15 fresh | 84.0 | 87.6 | 3.6 | 2.1 | 0.0113 |
| Au-0.6Mdp/SBA-15 spent | 83.8 | 87.4 | 3.6 | 1.8 | 0.0097 |
| Au-P/SBA-15 fresh | 84.0 | 87.5 | 3.5 | 1.8 | 0.0036 |
| Au-P/SBA-15 spent | 79 | 82.5 _____ 87.5 | | | |
| Au-0.6Adp/SBA-15 fresh | 84.3 | 87.9 | 3.6 | 2.0 | 0.0023 |

As seen in Table 1, the Au/Si ratio (surface) is slightly different between the fresh and spent samples. Whereas the Au/Si ratio increases from fresh to spent Au-en/SBA-15 catalyst, the Au/Si ratio decreases from the fresh to spent Au-0.6Mdp/SBA-15 catalyst. A possible explanation for their different behaviour lies on the different particle size of the fresh samples and their different susceptibility to sintering. The particle size for the fresh catalyst's samples was determined via TEM and XRD (see Table 2). The average particle size for the Au-en/SBA-15 sample was 60 Å, whereas for the Au-0.6Mdp/SBA-15 one, it was 19 Å. As claimed in the literature [37], particles with a very small size (diameter < 30 Å) are expected to be mobile and to migrate through surface diffusion when the temperature increases, leading to coalescence when particles come in close proximity to each other. As such, some of the small surface Au particles of the Au-0.6Mdp/SBA-15 sample will disappear, leading to a decrease in the Au/Si surface ratio. As for the particles with a diameter between 30 and 100 Å, their mobility decreases with the increase in size, which slows down the sintering process, and subsequently, the Au/Si surface ratio would not be affected in a negative way. What is more, some of the smaller particles can migrate from the pores to the surface during reaction. Consequently, the Au/Si surface ratio for the spent Au-en/SBA-15 sample was slightly higher than the one for the fresh sample.

**Table 2.** Calculated total number of gold atoms and dispersion for the fresh samples.

| Sample | Mean Diameter, D (Å) | | Total Number of Gold Atoms | Dispersion (%) |
|---|---|---|---|---|
| | TEM | XRD | | |
| Au-en/SBA-15 | 60 | 59 | 6650 | 22 |
| Au-0.6Mdp/SBA-15 | 19 | 19 | 211 | 58 |
| Au-0.6Adp/SBA-15 | 214 | 220 | $3 \times 10^5$ | 6 |
| Au-P/SBA-15 | 556 | 558 | $5.3 \times 10^6$ | 2 |

The H$_2$-TPR for all the fresh samples started off at room temperature, with readings measured from around 50 °C, and gradually rose to 500 °C at the 10 °C/min ramp rate. Hydrogen and water MS partial pressures signals drifted continuously with no observed hydrogen consumption peak with corresponding water formation peak, which suggests that no observable reduction occurred between 50–500 °C for all Au/SBA-15 samples.

H$_2$-TPR measurements (see Figure 2) however, show some hydrogen consumption but only at temperatures lower than 150 °C, which could be due to the physical adsorption of hydrogen. The amount of effluent H$_2$ stays constant for temperatures higher than 150 °C. This behaviour could be attributed to the incomplete evacuation of hydrogen, a very small molecule, from the ionisation chamber of the mass spectrometer. As no hydrogen consumption was observed at higher temperatures and almost no water was formed, one

can conclude that no reduction of the gold species occurred, or, in other words, the gold species were already reduced, i.e., $Au^0$ at room temperature.
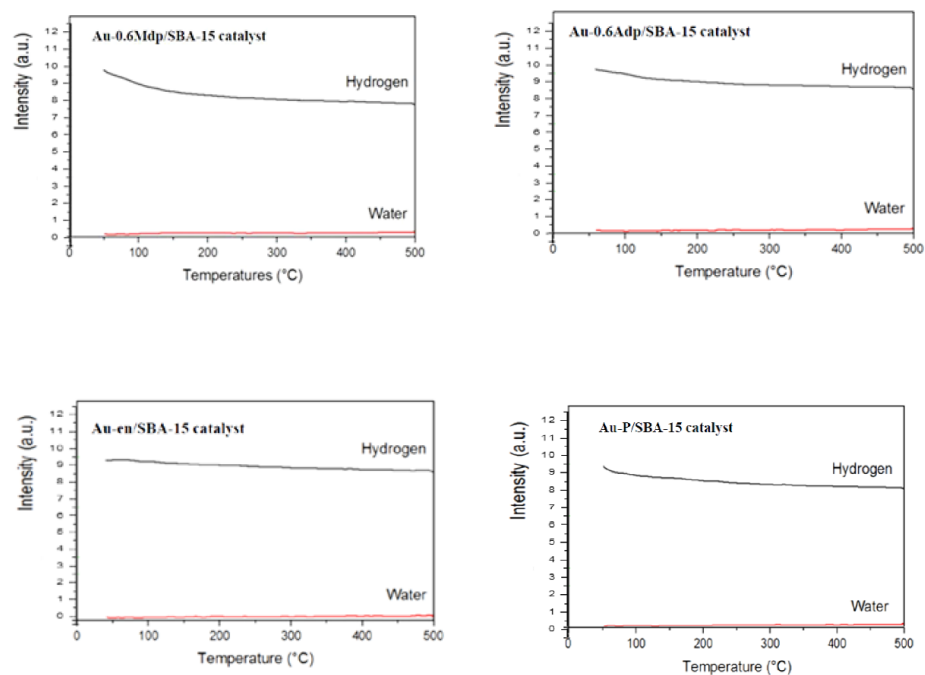


**Figure 2.** $H_2$–Temperature Programmed Reduction of the fresh samples.

The size of the gold particles and their dispersion on SBA-15 was assessed by TEM measurements and data analysis.

Figure 3a–g presents the TEM images taken on the fresh and spent samples. Each histogram was obtained by measuring the particle size for more than 1000 particles from 30 to 40 TEM images for each sample. The diameter of the gold nanoparticles was analysed using the image analysis software, ImageJ (NIH).



(a)

(b)

**Figure 3.** *Cont.*
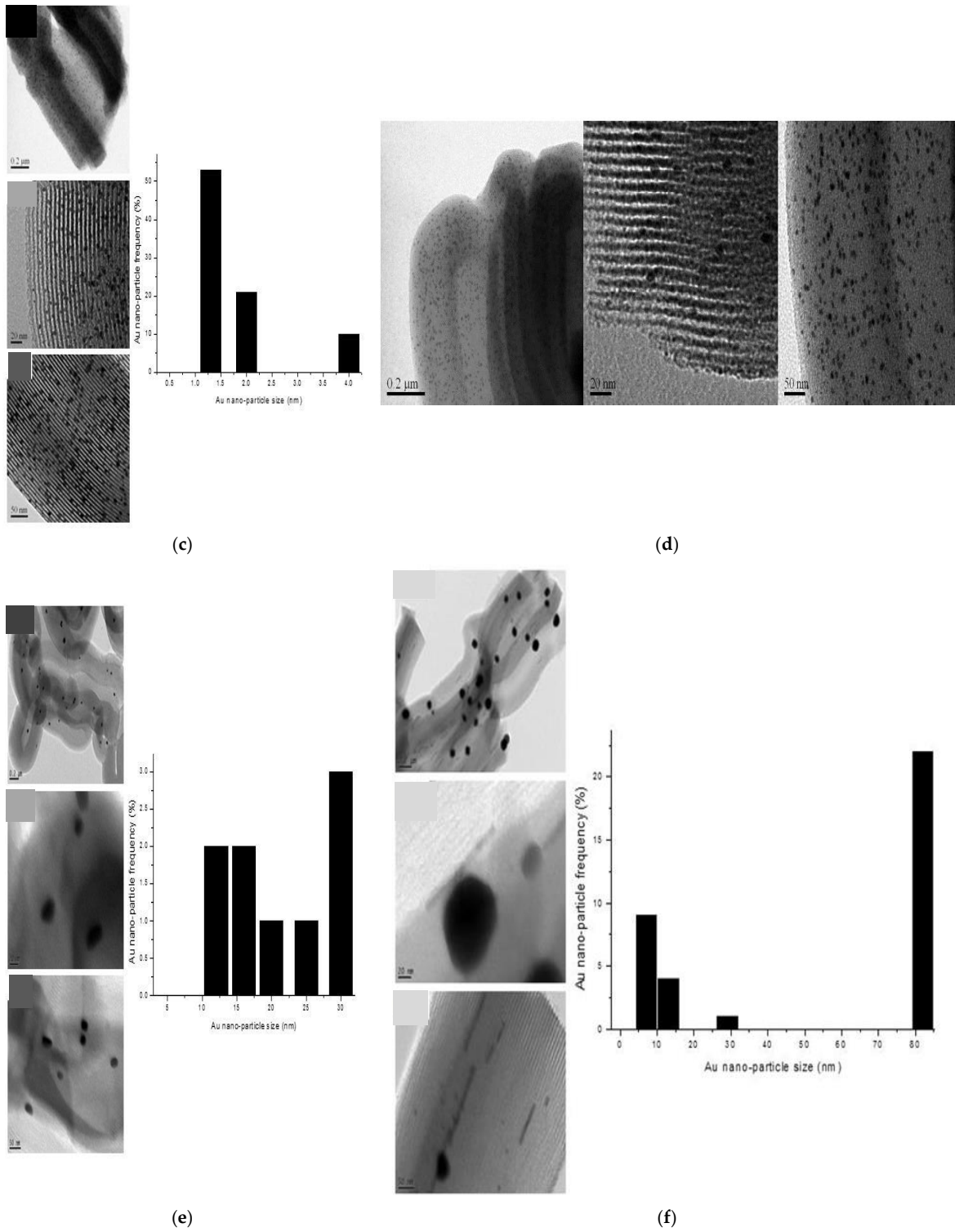
(**c**)

(**d**)



(**e**)
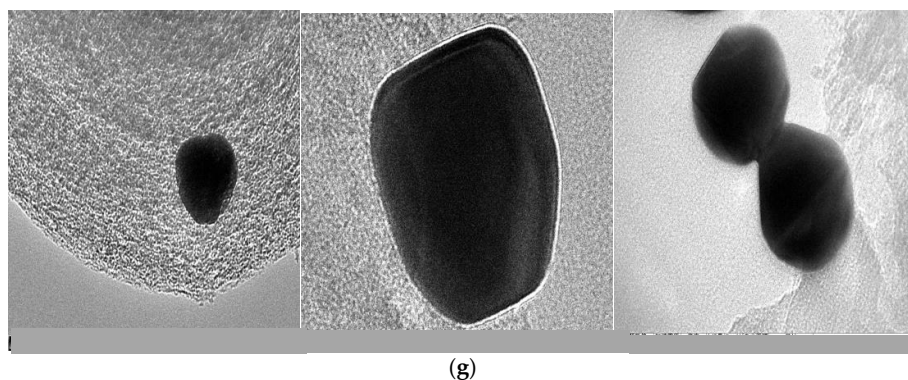
(**f**)

**Figure 3.** *Cont.*

(**g**)
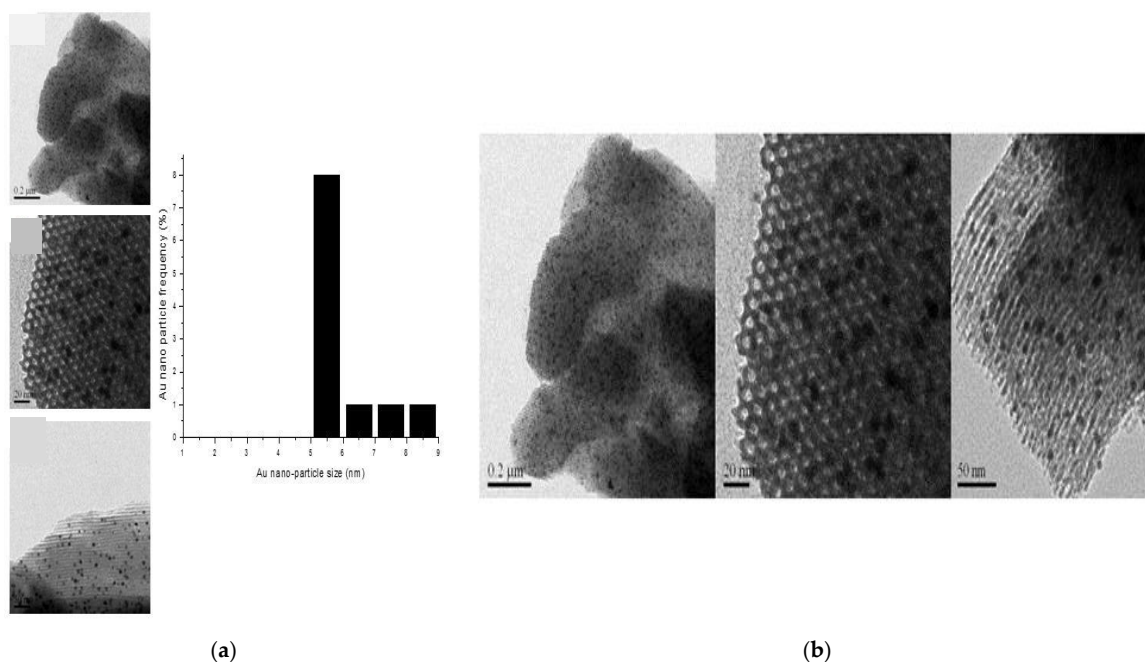
**Figure 3.** (**a**). TEM images and Au particle size distribution of fresh Au-en/SBA-15; mean size 60 Å; (**b**) TEM images of spent Au-en/SBA-15; (**c**) TEM images and Au particle size distribution of fresh Au-0.6Mdp/SBA-15; mean size 19 Å; (**d**) TEM images of spent Au-0.6Mdp/SBA-15; (**e**) TEM images and Au particle size distribution of fresh Au-0.6Adp/SBA-15; mean size 214 Å; (**f**) TEM images and Au particle size distribution of fresh Au-P/SBA-15; mean size 556 Å; (**g**) TEM images of spent Au-P/SBA-15.

TEM micrographs clearly reveal the size, shape, and location of the gold nanoparticles.

For the Au-en/SBA-15 and Au-0.6Mdp/SBA-15 fresh samples, a great majority of the particles have been successfully entrapped inside the SBA-15 channels and show spherical morphology (Figure 3a,c).

The smallest gold particles were observed for the Au-0.6Mdp/SBA-15 fresh sample (Figure 3c). They were well-dispersed and very stable as the TEM taken after their use in the acetone oxidation reaction showed no significant sintering (Figure 3d). Furthermore, no significant changes of the size and the shape of the gold particles were observed for the used Au-en/SBA-15 sample (Figure 3b).

For the Au-0.6Adp/SBA-15 fresh sample, TEM micrographs show bigger gold particles, some still spherical, some oval-shaped, and with the majority of them at the external surface of the support.

TEM images of the Au-P/SBA-15 fresh sample (Figure 3f) reveal the formation of rather elongated 1D particles inside the pores along with bigger irregularities in shape 3D particles, and on the surface of the support. As for the Au-P/SBA-15 spent sample (Figure 3g), TEM micrographs show mostly bigger 3D surface particles.

TEM images taken over the Au-P/SBA-15 spent sample (Figure 3g) confirmed that the two chemical environments for $Au^0$, Au-Au clusters were on top of each other and on the surface of the support, as predicted by XPS measurements.

The mean particle size was calculated and the results are presented in Table 2.

As shown by the TEM images (Figure 3a,b), the hexagonal ordered mesoporous structure of SBA-15 was not altered, neither by gold loading nor by an oxidation reaction. Dispersion is slightly different from sample to sample as it depends on the particle size, which in turn depends on the number of gold atoms in the clusters. The total number of gold atoms, $N_{Au}$, is commonly calculated assuming a quasi-spherical gold nanoparticle shape using Equation (1) [38,39]:

$$N_{Au} = \frac{\pi D^3}{102} \tag{1}$$

where $D$ is the diameter of the gold nanoparticle in Å.

The number of gold atoms at the surface is calculated from the volume difference between the particle and the particle with one surface layer less, which has the radius to be $(D/2–d)$. $d$ and has a layer spacing of Au 2.38 Å.

Table 2 presents the calculated total number of gold atoms for each of the samples, along with the calculated dispersion.

As the SBA-15 average pore diameter was 54 Å, and as gold loading did not affect the pore size, one can conclude that the prepared samples can be divided into two groups: (i) small Au particles inside the support's pores, and (ii) with large Au particles (clusters) on the external surface of the support.

The nature and the size of the Au nanoparticles along with Au dispersion were also assessed through EXAFS and XRD measurements and data analysis. As seen in Figure 4, for all tested samples, metallic gold only was identified from the EXAFS spectra taken against the Au foil.
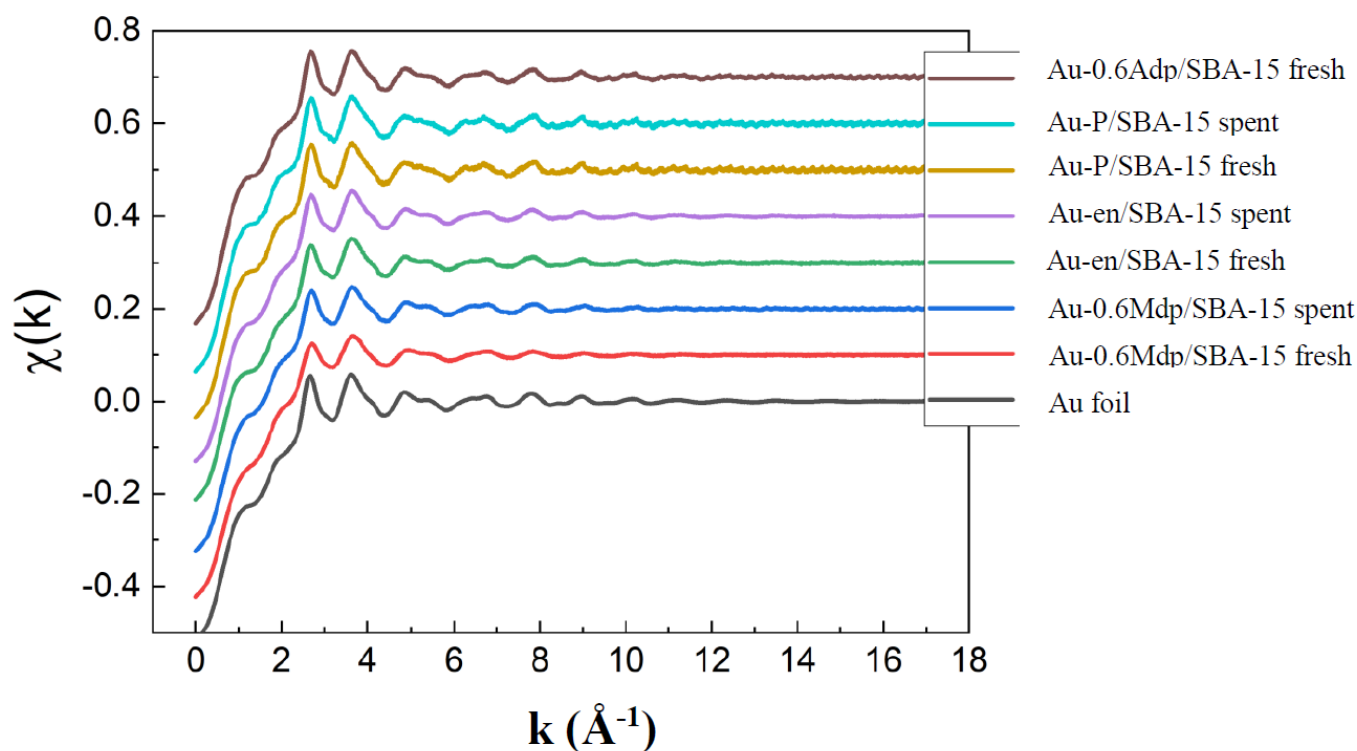


**Figure 4.** EXAFS spectra of all Au/SBA-15 samples.

For all samples, the typical features for Au-Au peaks were observed between 2 and 4 Å (Figure 5). However, the features are largely distorted for the Au-0.6Mdp/SBA-15 samples. This is mostly likely due to a stronger interaction with the support. During the preparation of the Au-0.6Mdp/SBA-15 sample, Au first interacted strongly with the -SH function on the SBA-15 inner wall, which regulated the migration of Au to reduce the aggregation. It was found that on the -SH modified oxide surfaces, Au was atomically dispersed, as sulphur atoms formed strong covalent bonds with Au to produce stable surface complexes. Consequently, the size of the Au particles was the smallest. The similar kind of retardation of Au aggregation was seen for the Au-en/SBA-15 sample where Au was attached to the oxygen atoms on the surface, -O-Si. However, the Au-O interaction was much weaker than the Au-S one. As a result, Au was able to migrate more easily and to aggregate to larger particles. One can conclude that the Au structure can be controlled by the surface modification method [40,41].

Moreover, there are slight changes in the Au-Au distance from sample to sample. The shortest $R_{Au-Au}$ seems to be for the samples with the smallest particle size, i.e., the Au-0.6Mdp/SBA-15 ones. Our finding is in good agreement with the literature data. Miller et al. [42] established a relationship between the gold particle size and the Au-Au bond length. The smaller the particle size, the shorter the Au-Au bond length. Theoretical calculations for small Au clusters sustain the shortening of the Au-Au distance with decreasing cluster size [43].
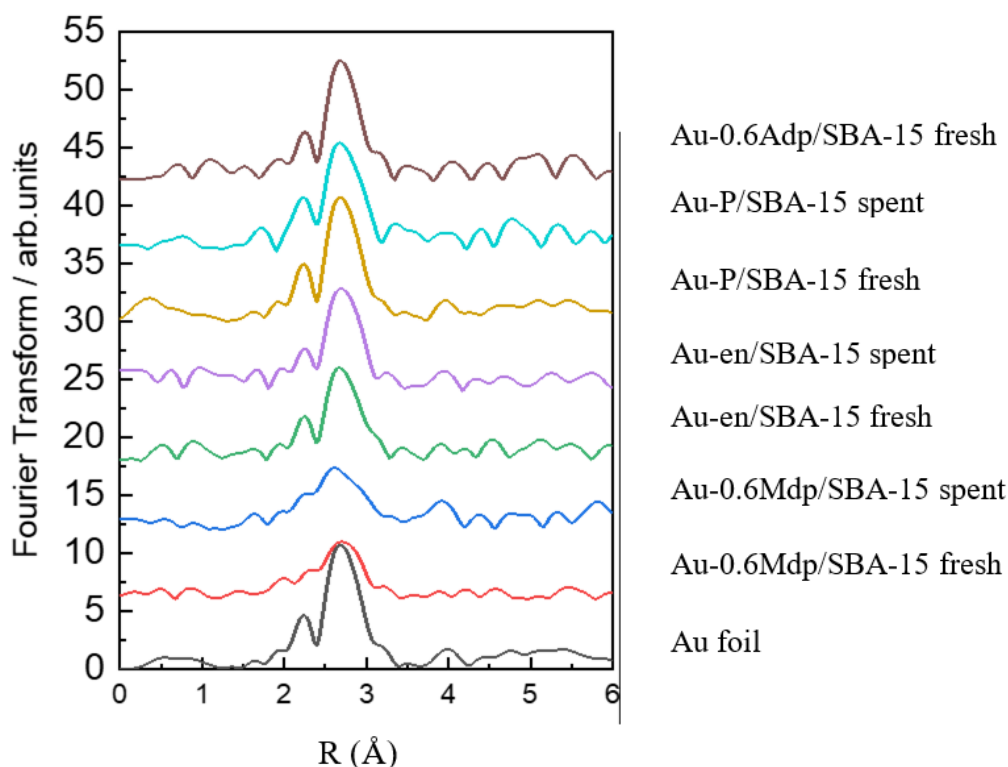
**Figure 5.** Magnitude of the $k^3$-weighted Fourier transformed EXAFS data for all samples.

In Figure 10 [42], for a particle size of 19 Å (Au-0.6Mdp/SBA-15 fresh), the Au-Au bond length is 2.85 Å, whereas for a particle size of 60 Å (Au-en/SBA-15 fresh), the Au-Au bond length is about 2.87 Å, results that are in good agreement with the EXAFS fitting data (Table 3).

**Table 3.** Structural parameters as revealed from EXAFS data analysis.

| Sample | $N_{Au-Au}$ (CN) | $R_{Au-Au}$ (Å) | DW (Å$^2$) |
|---|---|---|---|
| Au foil | 12.0 | 2.88 | 0.060 |
| Au-0.6Mdp/SBA-15 fresh | 8 ± 3 | 2.86 ± 0.01 | 0.07 ± 0.02 |
| Au-0.6Mdp/SBA-15 spent | 10 ± 3 | 2.87 ± 0.01 | 0.08 ± 0.02 |
| Au-en/SBA-15 fresh | 9 ± 2 | 2.88 ± 0.01 | 0.06 ± 0.01 |
| Au-en/SBA-15 spent | 10 ± 2 | 2.88 ± 0.01 | 0.06 ± 0.01 |
| Au-P/SBA-15 fresh | 11 ± 1 | 2.87 ± 0.01 | 0.06 ± 0.02 |
| Au-P/SBA-15 spent | 11 ± 1 | 2.88 ± 0.01 | 0.06 ± 0.02 |
| Au-0.6Adp/SBA-15 fresh | 11 ± 1 | 2.88 ± 0.01 | 0.06 ± 0.02 |

The Au particle size for all samples was calculated using the correlation between the coordination number and the particle size, following the method described by [44]. The average particle size calculated for the Au-0.6Mdp/SBA-15 fresh sample is in good agreement with the values determined from XRD and TEM measurements, i.e., 14 Å compared to 19 Å.

As expected, the dispersion increases with the decrease in particle size (Table 2). For Au catalysts with dispersion lower than 50%, almost no changes in the bond length relative to Au foil occurred (Tables 2 and 3). For the Au-0.6Mdp/SBA-15 fresh sample, for which the calculated dispersion was higher than 50%, i.e., 53%, the maximum contraction of the Au bond distance was significantly larger, e.g., about 0.03 Å.

Data analysis through fitting in *k*-space, with fixed $E_0$ and Au foil as references, generated the following results (Table 3).

The wide-angle XRD patterns of the four fresh catalysts are shown in Figure 6. The catalysts exhibit four diffraction peaks at $2\theta \sim 38.2°$, $44.3°$, $64.5°$, and $77.5°$, which are indexed to Au (111), Au (200), Au (220), and Au (311) reflections, respectively, for the face-centred cubic (FCC) lattice structure of Au (JCPDS file number: 04-0784). The Au-0.6Mdp/SBA-15 catalyst shows only a small broad peak at $38.2°$, an indication that the gold nanoparticles are very small. For the other three samples, the peaks are sharp and intense, indicating good crystallinity of metallic Au. The crystallite size for all samples was calculated from Scherrer's equation and is reported in Table 2. As expected, there are no significant differences between the gold particles' size measured by TEM and XRD.
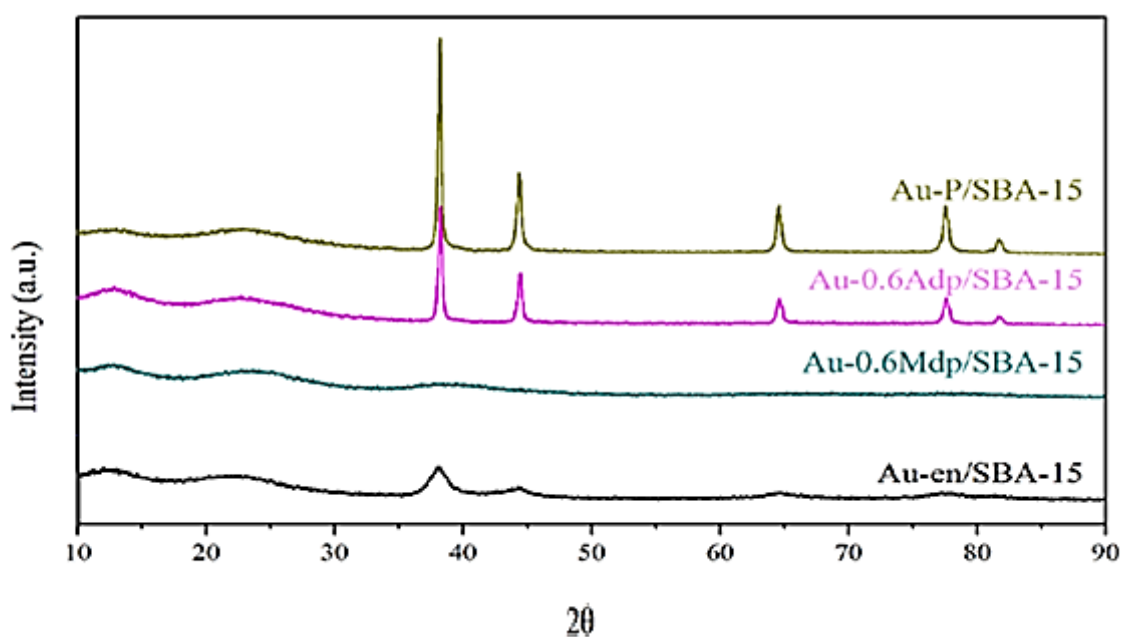


**Figure 6.** Wide-angle XRD of the fresh samples.

For TAP experiments, only the Au-0.6Mdp/SBA-15 catalyst sample was chosen.

TAP measurements were employed to study the reducibility of the sample, the adsorption of active species, i.e., acetone and oxygen, the catalytic activity, if any, the lifetime of adsorbed intermediates, and to propose the reaction mechanism.

Firstly, the reducibility of the gold species was qualitatively assessed after sending several pulses of $H_2$ over the catalyst at RT, 100, 200, 300, 400, and 450 °C. As seen in Figure 7, there is some interaction between the hydrogen and the catalyst, and it was slightly different from temperature to temperature. Conclusive evidence that there is indeed a $H_2$–catalyst interaction is obtained by comparing the $H_2$ response when pulsed in an empty microreactor with that of $H_2$ response over the catalyst (see Figure 7-Inset). If oxidized gold species were present and chemical adsorption leading to the reduction of these gold species occurred, then the $H_2$ response curves would be broader as the temperature of measurements was increased (activated adsorption). The higher the temperature, the stronger the interaction and the broader the response curve. However, as the response curves does not broaden after 300 °C, one can conclude that weak (physical) adsorption mainly occurred. As no chemisorption leading to the reduction of the gold species occurred validates the TPR and XRD findings that the active site is metallic gold ($Au^0$). As observed in Figure 2, there is a slight $H_2$ consumption over the Au-0.6Mdp/SBA-15 sample, increasing as the temperature is increased from RT to 300 °C, most probably due to physical adsorption on the catalyst's pores, but levelling up as temperature is increased from 300 to 450 °C. No $H_2$ consumption

at temperatures higher than 300 °C means there was no chemical or activated adsorption, therefore there was no reduction of the catalyst.
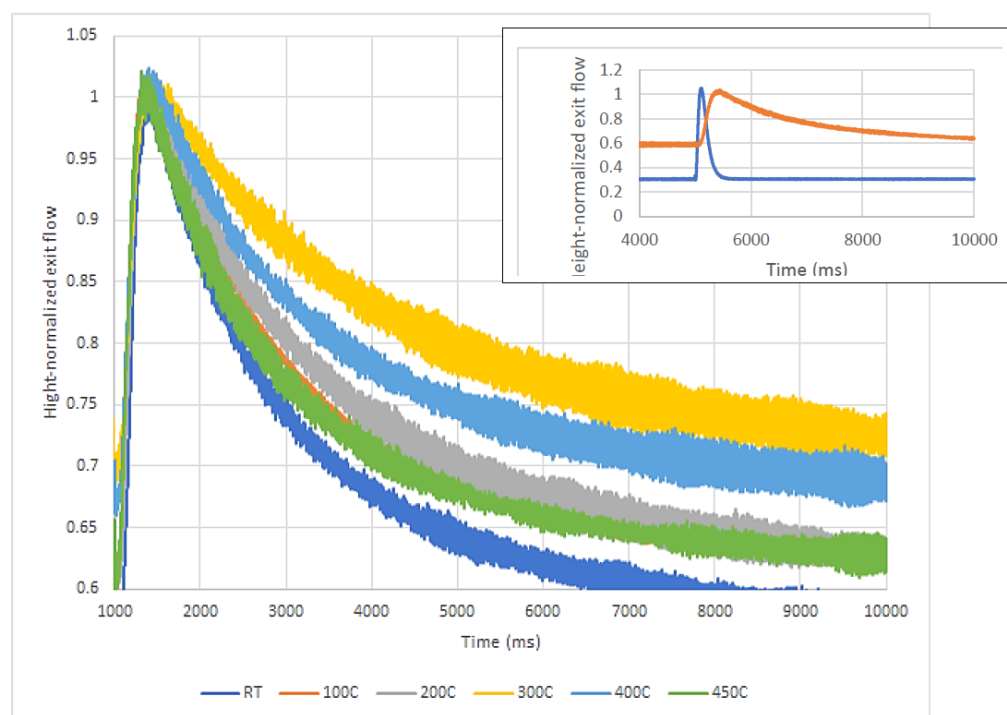


**Figure 7.** $H_2$ response to $H_2$ single-pulse experiments at RT, 100, 200, 300, 400, and 450 °C over the 5 mg catalyst. Inset: $H_2$ response to $H_2$ single-pulse experiments at RT in empty (blue) and microreactor filled with 5 mg catalyst (orange). Note: The main and the inset figures have a different time origin because when the experiments were performed over the empty microreactor, the delay between the pulses was set at 5000 ms only, whereas when experiments were performed over the microreactor filled with catalyst, the delay between the pulses was set at 1000 and 5000 ms.

Along with the $H_2$ interaction with the catalyst, the acetone interaction was studied as well, from acetone response to acetone/Ar single-pulse experiments at RT, 100, 200, 300, 400, and 450 °C. The acetone in the Ar mixture was obtained by flowing pure Ar over a small cylinder containing acetone at RT and the composition was determined from the responses of acetone and Ar at RT in an empty tube, as there was 10% acetone in Ar. Figure 8 shows all acetone responses. At RT and 100 °C, the acetone responses are very broad; there is almost no acetone leaving the microreactor. The acetone responses become narrower, and the peak appears earlier as the measurement temperature increased.

The quantitative analysis of the $H_2$ and acetone responses was performed using the moment-based approach [45]. One of the main features of the TAP curves, the mean residence time, $t_{res}$, was calculated as the ratio between the first and zero-th moment (area under the curve). Table 4 presents the calculated values of $t_{res}$ at measurement temperatures.

The quantitative results confirm the qualitative ones regarding the interaction between the active gases and the catalyst; the longer the residence time, the stronger the interaction of the gases with the catalyst. For hydrogen, the residence time increases as temperature is increased up to 300 °C, and then decreases as temperature is increased further. This pattern can be explained again by weak hydrogen-catalyst interactions, through physical adsorption mainly and some possible surface $OH^-$ reduction.
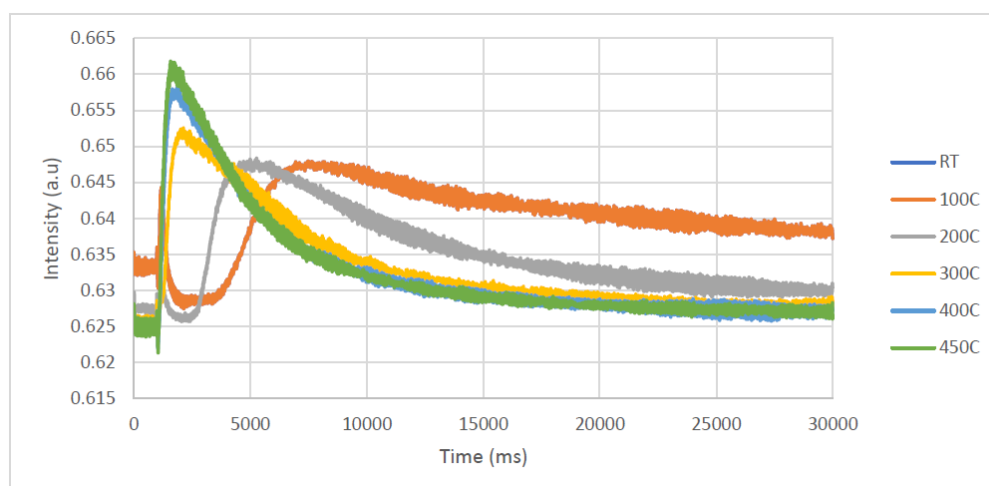
**Figure 8.** Acetone response to acetone/Ar single-pulse experiments at RT, 100, 200, 300, 400, and 450 °C over the 5 mg catalyst.

**Table 4.** Calculated residence time for $H_2$, acetone, and Ar responses in an empty TAP reactor along with their responses over the catalyst at RT, 100, 200, 300, 400, and 450 °C.

| Species | Residence Time (ms) | | | | | | |
|---|---|---|---|---|---|---|---|
| | **Empty Reactor** | **RT** | **100 °C** | **200 °C** | **300 °C** | **400 °C** | **450 °C** |
| Hydrogen | 208 | 1748 | 2844 | 3268 | 3680 | 2833 | 2439 |
| Acetone | 305 | 5630 | 14,834 | 10,630 | 7814 | 7311 | 6932 |
| Argon | 258 | 2312 | 7804 | 9924 | 9337 | 7922 | 7336 |
| $t_{res\ acetone}/t_{res\ Ar}$ | 1.2 | 2.4 | 1.9 | 1.1 | 0.8 | 0.9 | 0.9 |
| $t_{res\ hydrogen}/t_{res\ Ar}$ | 0.8 | 0.75 | 0.4 | 0.3 | 0.3 | 0.4 | 0.3 |

For acetone, the time spent in the TAP reactor increases as the temperature is increased up to 100 °C, and then decreases as the temperature is increased step-by-step up to 450 °C. One can conclude that there is some adsorption of acetone on the catalyst at low temperatures, which is most probably due to the weak, physical adsorption. As the pulse size was extremely narrow, i.e., around $1 \times 10^{15}$ molecules/pulse, the gas transport inside the microreactor is assured by Knudsen diffusion [46]. In this situation, the ratio between the residence time of acetone and the residence time of Ar is inversely proportional to the ratio between their respective diffusion coefficients, which is directly proportional to the square root of their respective molecular mass ratio [47,48].

$$\frac{t_{res\ acetone}}{t_{res\ Ar}} \sim \frac{D_{Ar}}{D_{acetone}} \sim \sqrt{\frac{M_{acetone}}{M_{Ar}}} \qquad (2)$$

If only Knudsen diffusion occurs, then the $\frac{t_{res\ acetone}}{t_{res\ Ar}} = 1.2$.

However, as seen in Table 1, for low temperatures, RT and 100 °C, the above ratio is much higher than 1.2, which means that acetone spends more time in the microreactor because of weak (most probably physical) adsorption. For higher temperatures, this ratio approaches the one calculated based on Knudsen diffusion only, which supports the assumption that acetone is not strongly adsorbed on the surface.

Following the same reasoning, if only Knudsen diffusion occurs when hydrogen is passed over the catalyst, then the ratio between the hydrogen residence time and argon residence time should be 0.22. However, at RT, the ratio is much higher, whereas at higher temperatures than RT, the ratio stays almost constant, which corroborates the TPR results,

which showed some hydrogen "consumption" from RT to 100 °C, which is most probably due to physical adsorption.

To study the catalytic activity of the Au-0.6Mdp/SBA-15 sample, single-pulse experiments with oxygen:acetone/Ar mixtures were performed at RT, 100, 200, 250, and 300 °C. The responses of $O_2$ and acetone were recorded, both from their respective pulses, to assess their adsorption behaviours, and from their mixture pulses as well, to assess changes, if any, in their behaviour, or changes related to their interactions with catalyst or between them. The $CO_2$ response was also recorded from the mixture pulse.

As seen in Figure 9, there is a significant difference in the $O_2$ adsorption's features at RT when it is pulsed alone or in mixture with acetone. The result supports the assumption that there is a competitive adsorption occurring when oxygen and acetone are pulsed together, as the oxygen response in the acetone presence is much narrower than in the absence of it. The adsorption could occur on both the support and Au nanoparticles. However, as SBA-15 mesoporous silica belongs to the inert, so-called inactive supports, the adsorption of oxygen on the support's surface is excluded. Therefore, Au nanoparticles can be assessed as the active sites for oxygen and acetone adsorption and reaction.
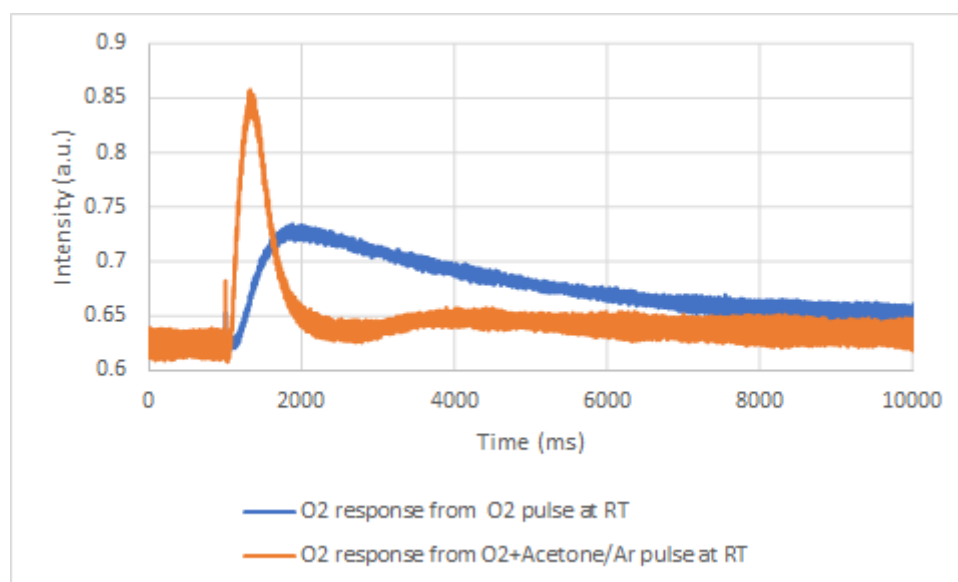


**Figure 9.** Oxygen response to oxygen and to oxygen:acetone/Ar mixture at RT over the 5 mg catalyst.

The quantitative data supports the competitive adsorption of oxygen and acetone as well. Oxygen spends more time in the microreactor (longer adsorbed) when it was pulsed alone than when it was pulsed together with acetone, i.e., 6538 ms compared to 5116 ms.

Differences similar to those observed at RT were revealed at the other temperatures as well. Figure 10a,b present the oxygen response as function of temperature, with A in the absence and B in the presence of acetone.

The small peak, around 4000 ms, shown on the oxygen response to oxygen:acetone/Ar mixture, at all temperatures, could be, most probably, attributed to a small amount of oxygen that was still adsorbed on the gold nanoparticles, despite the presence of acetone.

As shown in Figure 10a, there are not significant changes in the oxygen's response as a function of temperature. This behaviour prompts the conclusion that oxygen adsorption is not an activated one.

A careful examination of Figure 10b reveals that the peak slightly shifts to higher times as the temperature increases. Therefore, one can assume that the interaction of oxygen with the catalyst on which acetone was adsorbed (as concluded from Figure 9) becomes stronger, most likely because of the oxidation reaction.
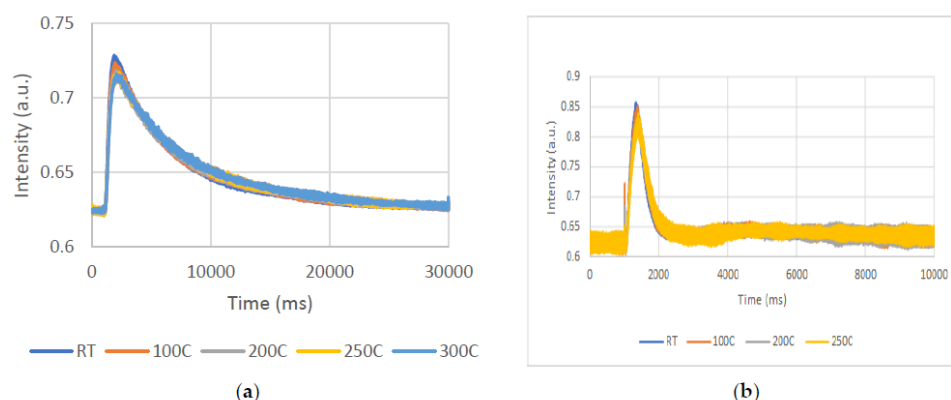
**Figure 10.** Oxygen response to: (**a**)–oxygen pulses and (**b**)–to oxygen:acetone/Ar pulses over the 5 mg catalyst.

Figure 11 presents the acetone response to oxygen: 10% acetone/Ar mixture pulse as a function of temperature.
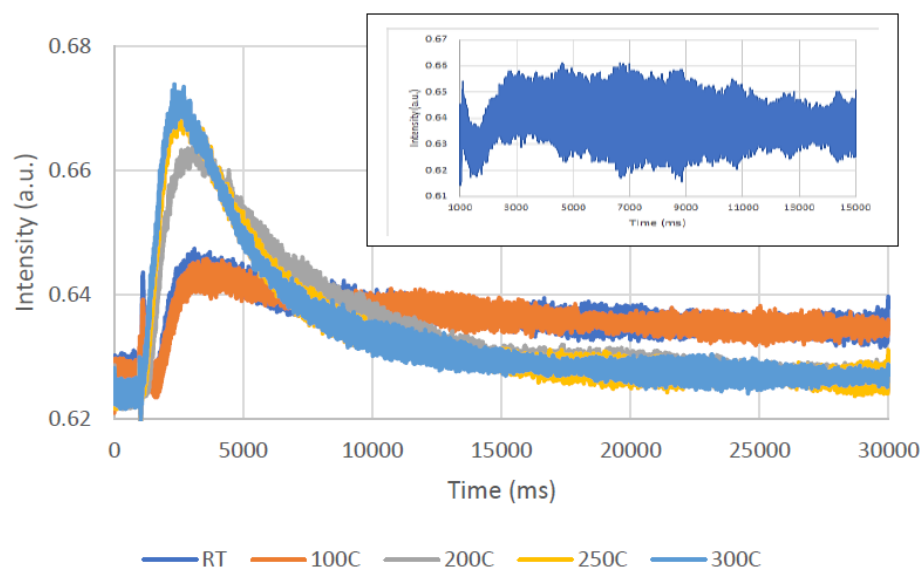


**Figure 11.** Acetone response to oxygen:acetone/Ar mixture single-pulse experiments at RT, 100, 200, 250, and 300 °C over the 5 mg catalyst. Inset: Acetone response at RT.

As expected, there is almost no acetone leaving the TAP reactor at RT, as acetone is physically adsorbed on the catalyst.

Undoubtedly clear evidence of the occurrence of the oxidation reaction could have been obtained by following the $CO_2$ response on the oxygen:acetone/Ar pulses, as a function of temperature. However, the $CO_2$ response was very noisy, even at 300 °C (not shown). The explanation for this is, on the one hand, that because of the low amount of acetone in the acetone/Ar pulse, only small amounts of $CO_2$ were produced, and, on the other hand, it is possible that the $CO_2$ formed was strongly adsorbed on the catalyst. Yang et al. [49] found that the BET surface area and the microporosity of a similar Au/SBA-15 catalyst were responsible for $CO_2$ adsorption. The higher the BET surface area and the microporosity, the higher the $CO_2$ uptake. As our catalyst has a rather high BET surface area of 726 $m^2/g$ and a high microporosity of 0.17 $cm^3/g$ [50], the noisy $CO_2$ response is most probably due to the strong adsorption of $CO_2$.

Another way to confirm whether the oxidation reaction occurred is to compare the experimental amount of acetone leaving the microreactor when oxygen:10% acetone/Ar mixture was pulsed, an amount which is directly proportional to the experimental zeroth moment, with the theoretical amount (i.e., no acetone consumption) calculated by

multiplying the zero-th moment of Ar response curves with the acetone/Ar ratio in the initial mixture.

Table 5 presents the results of this comparison at 200, 250, and 300 °C. At RT and 100 °C, there is almost no acetone leaving the reactor. As the difference between the Theoretical and Experimental zero-th moments of the acetone responses to the oxygen:10% acetone/Ar mixture pulses increases with temperature, one can conclude that the oxidation reaction occurred, with the acetone conversion increasing from 16% to 25%.

**Table 5.** Evidence of acetone oxidation reaction over the 5 mg catalyst at 200, 250, and 300 °C.

| Temperature (°C) | Acetone Response Experimental Zero-th Moment (V·s) | Acetone Response Theoretical Zero-th Moment (V·s) | Difference in Zero-th Moments (Theoretical–Experimental) (V·s) | Acetone Conversion % |
|---|---|---|---|---|
| 200 | 0.32 | 0.38 | 0.06 | 16 |
| 250 | 0.31 | 0.38 | 0.07 | 18 |
| 300 | 0.29 | 0.38 | 0.09 | 25 |

TAP pump-probe experiments were performed as well at 300 °C, at increased time intervals from 0 to 5000 ms. In order to assess the lifetime of adsorbed acetone, acetone was the pump molecule and oxygen the probe molecule. As seen in Figure 12, there was no more adsorbed acetone left after 1500 ms to react with the probe oxygen, as the oxygen responses after this time interval stay the same. The lifetime of adsorbed acetone is therefore less than 1500 ms. The oxygen responses were similar to those obtained when oxygen was pulsed alone (Figure 10A).
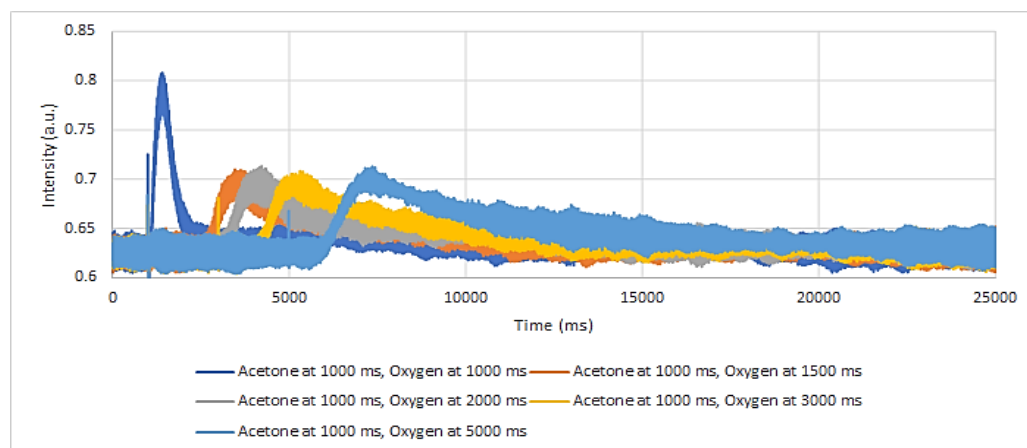


**Figure 12.** Oxygen responses (as probe molecule) as function of time interval, over the 5 mg of catalyst.

To assess the lifetime of adsorbed oxygen, TAP experiments with oxygen as the pump molecule and acetone as the probe molecule were performed. Figure 13 shows the acetone responses as a function of the time interval.
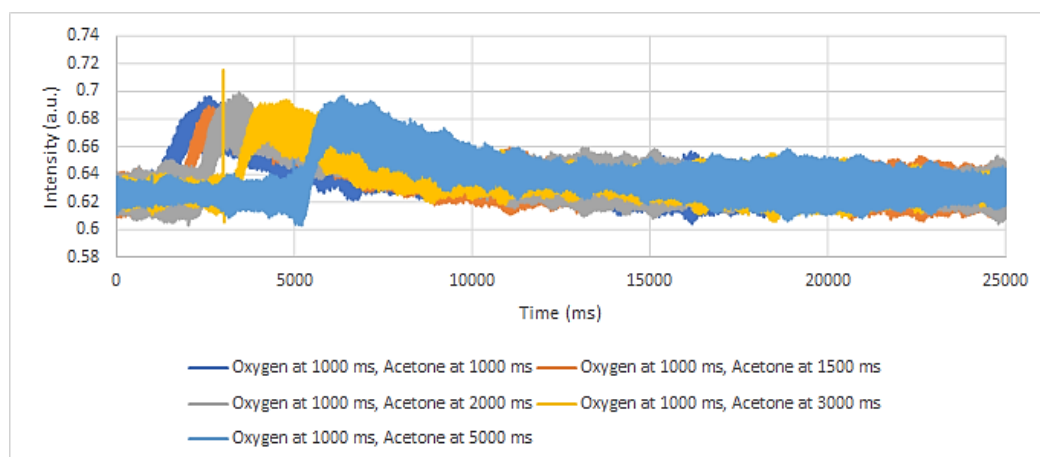
**Figure 13.** Acetone responses (as probe molecule, from acetone/Ar pulse)) as function of time interval over the 5 mg of catalyst.

Since there are no significant changes in the acetone response as the time interval increases, the TAP pump (oxygen)–probe (acetone/Ar) results confirm that oxygen does not adsorb on the catalyst when acetone is present.

Based on TAP results, one can conclude that the acetone oxidation reaction occurs mainly between acetone adsorbed on the Au nanoparticles and oxygen from the gas phase, likely following the Eley–Rideal mechanism, with a minor contribution of the reaction between both species adsorbed, following the Langmuir–Hinshelwood mechanism. Similar findings regarding the mechanism of acetone complete oxidation were revealed within the review by Mu et al. [31]. The acetone adsorption intermediates were shown as well. Figures 14 and 15 illustrate the two oxidation mechanisms [31]. The Eley–Rideal and Langmuir–Hinshelwood mechanisms are the two proven mechanisms for VOCs oxidation on non-reducible oxides supported by noble metals catalysts, whereas for the VOCs oxidation on reducible oxides that supported noble metals catalysts, the Mars–van Krevelan mechanism is generally accepted [4,12].
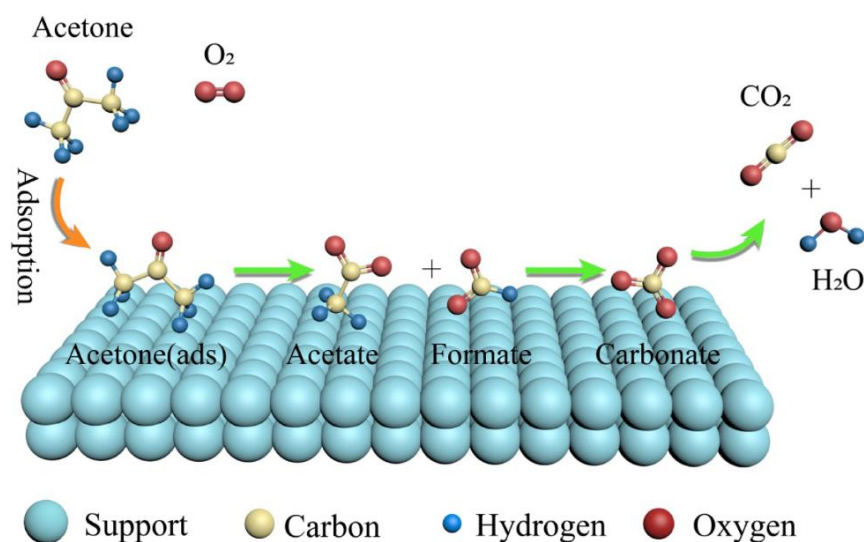


**Figure 14.** Eley–Rideal mechanism illustrated. Reprinted with permission from Mu et al., 2021, [31] Elsevier Ltd.
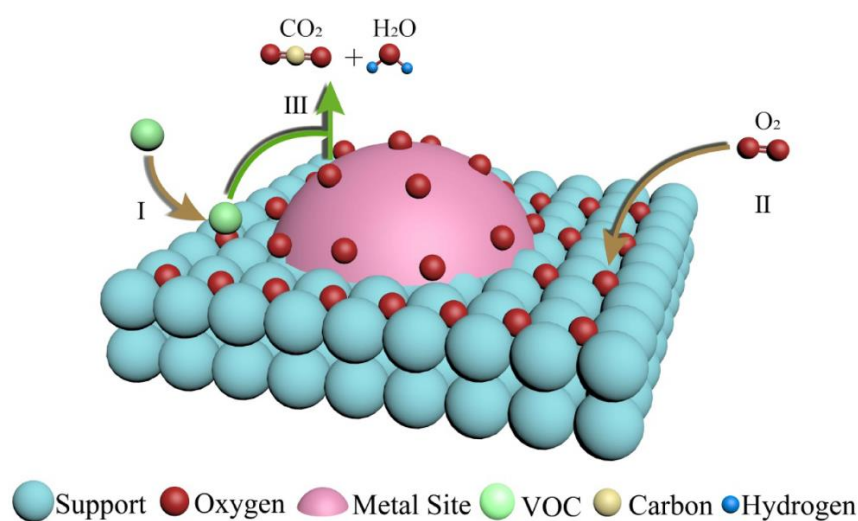
**Figure 15.** Langmuir–Hinshelwood mechanism illustrated. Reprinted with permission from Mu et al., 2021 [31], Elsevier Ltd.

The catalytic activity towards acetone oxidation of all samples was tested in a CFR.

By stoichiometry, one mole of acetone will produce three moles of $CO_2$ if 100% acetone conversion takes place by complete oxidation:

$$C_3H_6O + 4O_2 \rightarrow 3CO_2 + 3H_2O \tag{3}$$
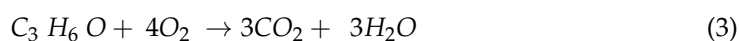
The acetone conversion was obtained from the MS signals. The plots for acetone conversion are shown in Figures 16–19.



**Figure 16.** Complete oxidation of acetone over oxidised and reduced Au-en/SBA-15 samples.

**Figure 17.** Complete oxidation of acetone over oxidised and reduced Au-0.6M dp/SBA-15 samples.



**Figure 18.** Complete oxidation of acetone over oxidised and reduced Au-0.6A dp/SBA-15 samples.

**Figure 19.** Complete oxidation of acetone over oxidised and reduced Au-P/SBA-15 samples.
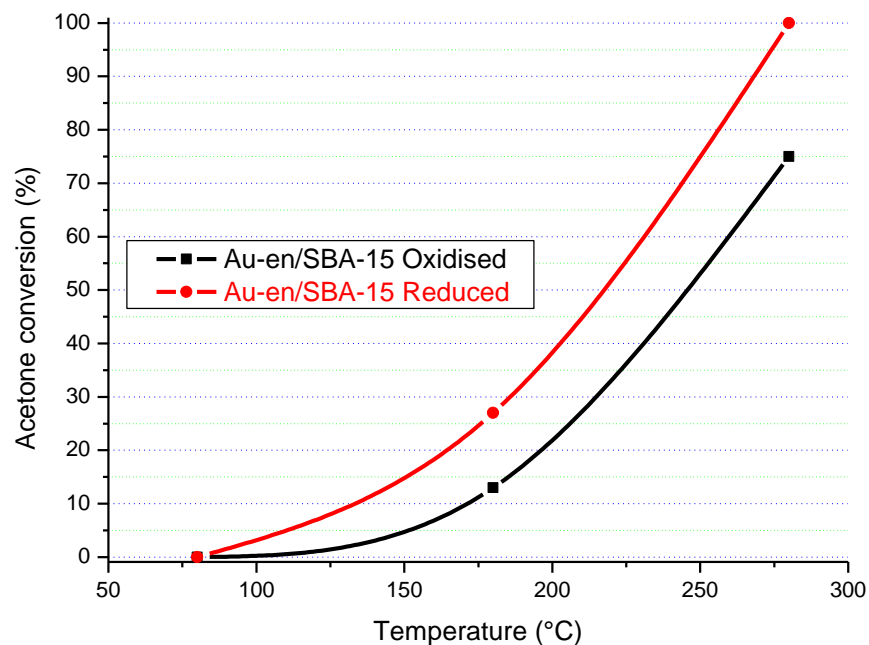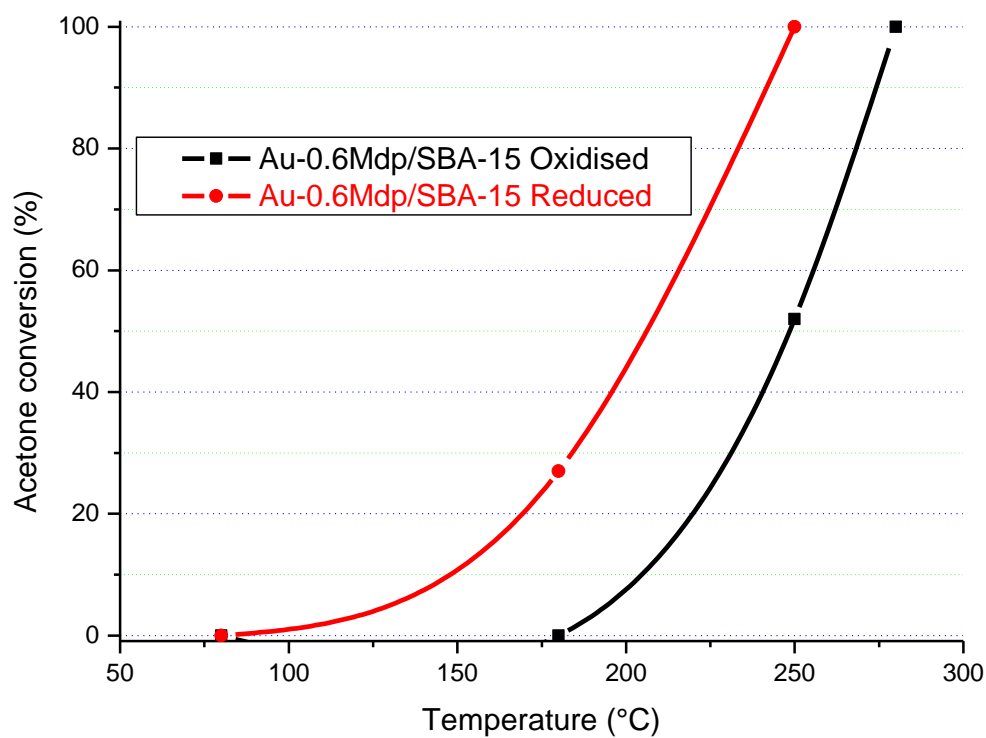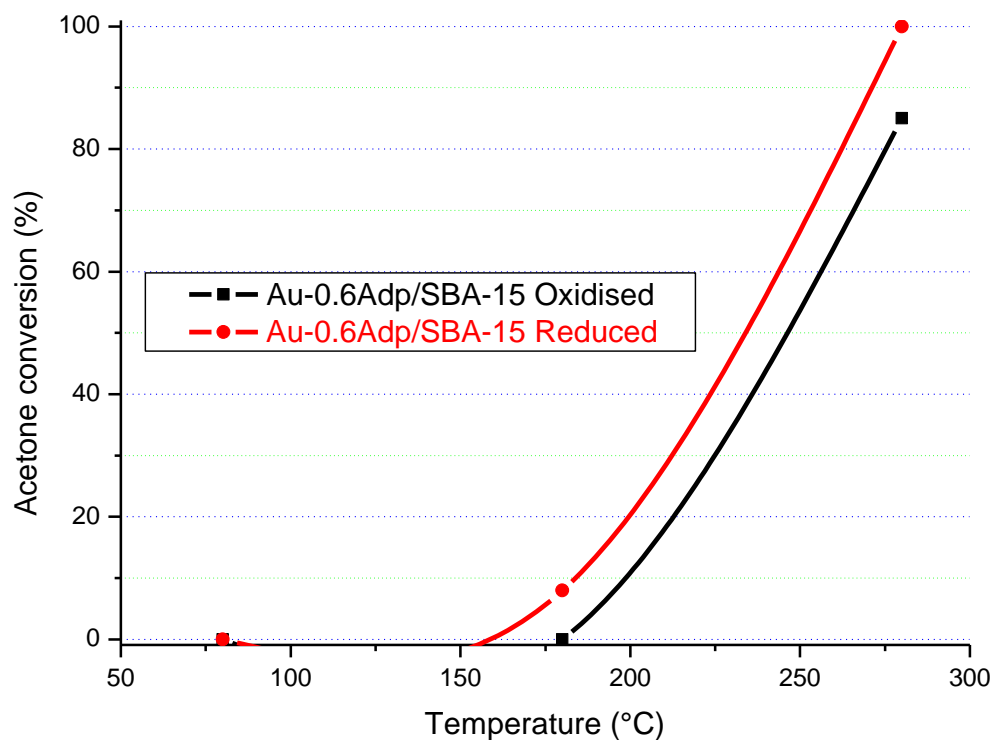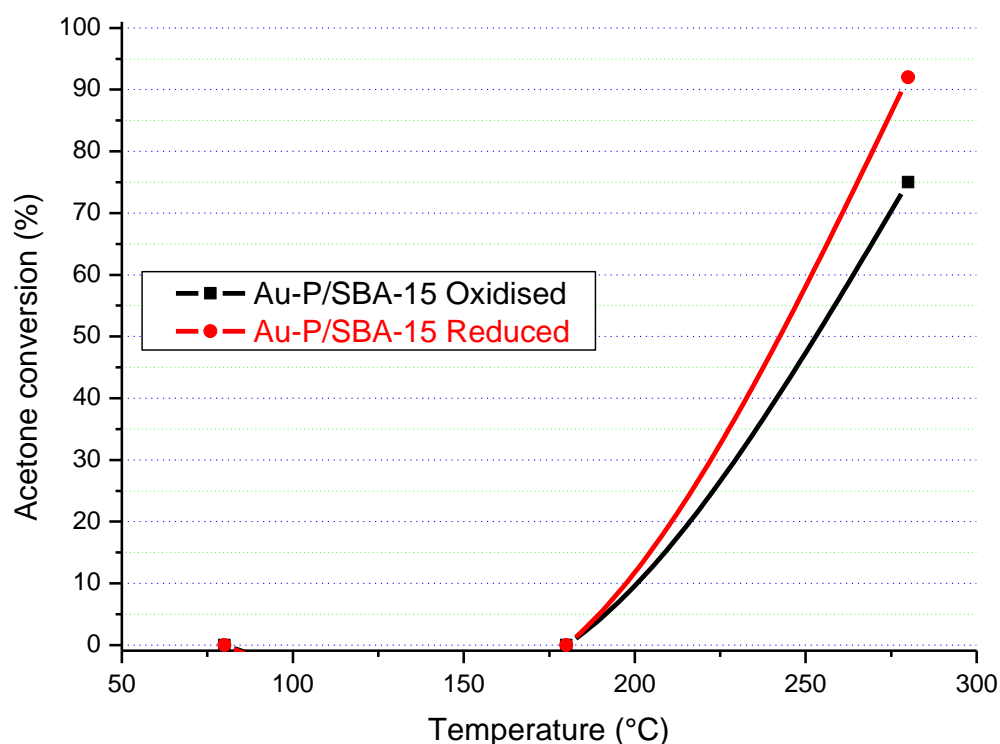
Two series of measurements were performed. The first series was performed over the catalyst's samples previously subjected to a flow of 60 mL/min 5% hydrogen in Ar at 500 °C for one hour (so called "Reduced") and the second series was performed over the as-synthesised samples (so called "Oxidised"). The pre-treatment in hydrogen led to the reduction of -OH groups still present on the samples' surfaces.

The acetone conversion–temperature plots are almost parallel for the oxidised and reduced samples indicates the same type of mechanism/kinetics for both forms.

The results in Figures 16–19 clearly show that the gold particle size and the state of the catalyst's surface had a significant influence on its catalytic activity. In terms of the state of the surface, there was a clear difference between the catalytic activity of the as-synthesised ("oxidised") and "reduced" Au/SBA-15 catalysts. Although both forms of Au/SBA-15 catalysts were highly active, the reduced catalysts showed higher catalytic activity, which indicates that a clean surface is beneficial.

The particle size of gold also influenced the catalytic activity. For instance, the Au-0.6Mdp/SBA-15 catalyst with most of its gold particle sizes at 1.3 nm (smallest gold particle size) was the only catalyst to attain 100% acetone conversion on Au/SBA-15 as-synthesised form at 280 °C. The other as-synthesised Au/SBA-15 catalysts only attained 75–83% acetone conversion at 280 °C. Furthermore, the reduced Au-0.6Mdp/SBA-15 sample proved to be the most active, attaining 100% acetone conversion at as low as 250 °C. The other reduced Au/SBA-15 catalysts, except for the reduced Au-P/SBA-15 catalyst, achieved 100% acetone conversion between 260–280 °C. The Au-P/SBA-15 catalyst with most of its gold particle sizes at 790 Å was the least active, attaining less than 100% (92%) at 280 °C. However, the presence of some smaller gold particle sizes (50–150 Å) in the Au-P/SBA-15 catalyst might have been responsible for its still high catalytic activity.

Therefore, the Au-0.6Mdp/SBA-15 catalyst with the smallest gold particle sizes (average of 1.9 nm), were well-dispersed and firmly attached to the SBA-15 support, and were provednto be the best Au/SBA-15 catalyst in the complete oxidation of acetone.

This sample not only showedthe highest catalytic activity towards acetone conversion, but, at the same time, it showed the highest reaction stability for catalyst lifetime tests

performed for 25 h in a CFR at 270 °C for the as-synthesised sample, and at 220 °C for the reduced sample.

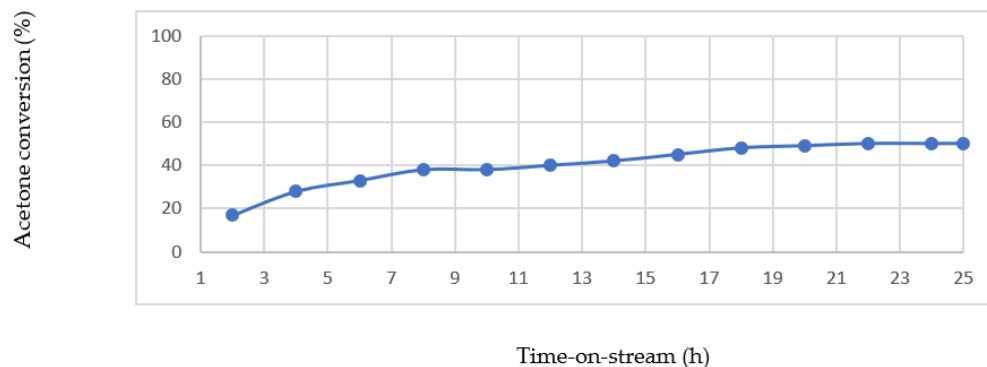The lifetime test results are shown in Figures 20 and 21.



**Figure 20.** Catalyst lifetime test for as-synthesised Au-0.6M dp/SBA-15 catalyst in acetone complete oxidation at 270 °C.
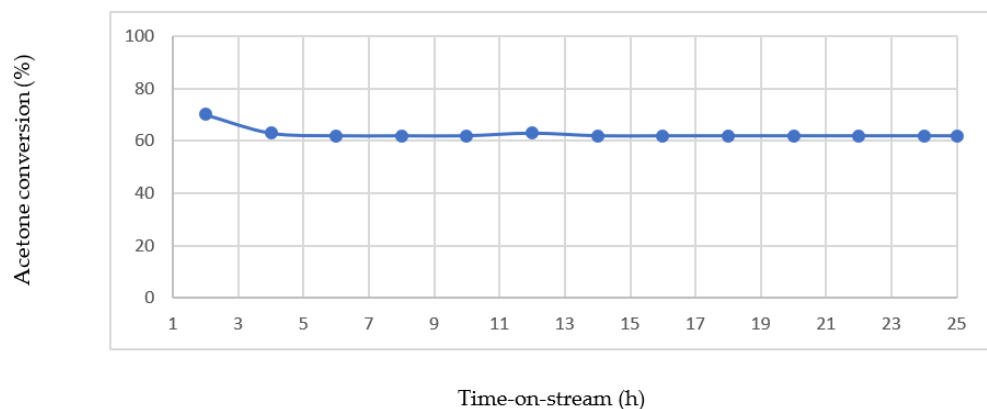


**Figure 21.** Catalyst lifetime test for reduced Au-0.6M dp/SBA-15 catalyst in acetone complete oxidation at 220 °C.

Stable operation of the as-synthesised Au-0.6Mdp/SBA-15 catalyst (Figure 20) was achieved after a period of about 18 h at about 50% acetone conversion. The result show there is a transient behaviour of the oxidised catalyst upon exposure to reaction stream. During this transient period, as explained by Avgouropoulous et al. [51], the carbon mass balance is deficient, indicating the deposition/adsorption of acetone-derived species on the catalyst surface. As soon as the catalyst surface is saturated, the carbon mass balance is satisfied, and the catalyst exhibits stable behaviour.

For the stability test of the reduced Au-0.6Mdp/SBA-15 sample (Figure 21), the observed increase in initial catalytic activity was about 4 h without a corresponding increase in $CO_2$ and $H_2O$. Gandía and et al. [52] experienced a similar trend in the complete oxidation of acetone over manganese oxide catalysts. They attributed the initial increase in catalytic activity in about 2 h to the possible retention of a significant amount of unreacted acetone in the catalyst (which explains why there was no observed increase in $CO_2$ and $H_2O$ formation that corresponding to the seeming increase in acetone conversion), which after saturating the catalyst surface, the reaction was stabilised. Further tests and characterisations may be required however to establish whether the observed initial increase in acetone conversion is as a result of the adsorption of unreacted acetone on the catalyst surface/stabilisation effect.

However, the catalyst stability test results shown in Figures 18 and 19 confirm that both the as-synthesised and reduced forms of Au-0.6M dp/SBA-15 catalyst remained highly

active and stable with no observed signs of catalyst deactivation over time-on-stream in the acetone complete oxidation reaction.

## 3. Experimental Section

### 3.1. Synthesis of SBA-15 Support

The general experimental procedure followed in the preparation of SBA-15 mesoporous silica was described in detail in the literature [24,25]. This procedure was modified, and the preparation conditions were optimised through experiments. The optimised procedure is described below.

4.0 g of tri-block copolymer of Poly (Ethylene Oxide)-Poly (Propylene Oxide)-Poly (Ethylene Oxide) ($EO_{20}PO_{70}EO_{20}$ or *Pluronic P123*, with a typical $M_n = 5800$), was dissolved in 130 mL deionised water. The formed solution was stirred continuously at 40 °C until it become transparent. Then, 20 mL HCl (37 wt%) was added, followed by the dropwise addition of 8.5 g of Tetraethyl Orthosilicate (TEOS). The reaction mixture was stirred moderately for 24 h, followed by aging at 80 °C for another 24 h without stirring. The white product was collected by filtration, dried, and then calcined at 500 °C for 6 h, with a heating rate of 1 °C/min. SBA-15 was then re-hydrated in boiling water for 2 h. The hydrated SBA-15 was dried at 130 °C for 3 h.

### 3.2. Synthesis of Au/SBA-15 Samples

The samples used in this study were synthesised using the following methods.

#### 3.2.1. Synthesis of Au-en/SBA-15 Catalyst (via Deposition-Precipitation)

An organic functional group was used to incorporate gold nanoparticles on the mesoporous silica material, starting with tetrachloroauric acid as a gold precursor for the synthesis of the cationic gold-organo-complex. Although active gold catalysts have been produced using this method, it may lead to some defects on the meso-structure due to the grafting of the organic functional groups and the ligand removal, with a high calcination temperature, leading to a decrease in catalytic activity. It was found that tetrachloroauric acid reacts with ethylenediamine (en) to form gold complex [Au $(en)_2]Cl_3$ after precipitation with ethanol. This complex behaves as an acid by losing a proton from the coordinated amine group under basic conditions [53]. The deposition-precipitation of this complex was carried out in alkaline media on the prepared SBA-15, as the negatively charged mesoporous silica material surface readily attracted the [Au $(en)_2]^{2+}$ cations by deprotonation reaction of the Au-ethylenediamine ligand [54]. The sample was labelled as Au-en/SBA-15. Both fresh and spent samples were characterised.

Firstly, the gold precursor, Au $(en)_2Cl_3$, was prepared using the method described in detail in the literature [54]. Afterwards, 2 g of $HAuCl_4 \cdot 3H_2O$ was dissolved in 20 mL deionised water and 0.90 mL ethylenediamine was slowly added and stirred for 30 min. Then, 140 mL ethanol was added, and the white suspension formed was stirred for 20 min and then filtered. The solid was washed with ethanol and dried in a vacuum at 40 °C overnight. To synthesise the Au-en/SBA-15 catalyst, 0.1 g of the cationic gold complex, Au $(en)_2Cl_3$, was dissolved in 50 mL water and the pH was adjusted to 10 using 0.1 M NaOH solution. A total of 1.0 g of SBA-15 was then added to the solution to form the Au-en-SBA-15 complex. The suspension was stirred at 65 °C for 2 h, filtered, and washed with deionized water. The product was dried in a vacuum at 70 °C for 5 h, then calcined at 500 °C for 6 h at 1 °C/min ramping to burn off the ethylenediamine ligand, leaving gold nanoparticles on SBA-15.

#### 3.2.2. Synthesis of Au-0.6Mdp/SBA-15 and Au-0.6Adp/SBA-15 Catalysts (via Co-Condensation)

One-pot functionalisation of SBA-15 with MPTMS (3-MercaptoPropyl) TriMethoxySilane) or APTMS ((3-AminoPropyl) TriMethoxySilane) was done as follows: 0.6 g of MPTMS or APTMS was added during the synthesis of SBA-15 2 h after the dropwise addition of

TEOS, and the reaction mixture was stirred moderately at 40 °C. When the synthesis was completed, the suspension was filtered under a vacuum, washed with deionized water, then with acetone, and dried at 80 °C overnight. P123 template removal from as-synthesised SBA-15-SH and SBA-15-NH$_2$ was done by Soxhlet extraction of 3.0 g of the functionalised SBA-15 into 200 mL of ethanol for 48 h. Recovered samples were dried at 60 °C for 24 h. 1.0 g of the functionalised support were and then suspended in 80 mL of distilled water and stirred for 30 min at 80 °C before adding 80 mg of HAuCl$_4$·3H$_2$O dissolved in 10 mL water. The solution gradually turned from light yellow to colourless within 5 min for MPTMS sample. After 20 min, the solution was cooled at room temperature for 20 min while stirring, then recovered by filtration, air dried for 18 h, and then kept at 60 °C for 24 h in an oven. The samples were finally calcined at 500 °C for 6 h at 1 °C/min ramping.

This method is also known as self-assembly functionalisation of SBA-15 before gold loading. As mentioned above, the organosilane (MPTMS or APTMS) was added directly during the SBA-15 synthesis. Co-hydrolysis and (poly)condensation of the silica precursor and organosilane takes place in the presence of P123 template. The advantage of this method is that homogeneous functionalisation can be achieved as the organosilane is part of the silica matrix, which also eliminates the issue of pore blockage. The disadvantage of this method is the difficulty in determining the right amount of organosilane enough to *functiona* lise SBA-15 without inhibiting the hydrolysis and condensation of the silica precursors, which affects the formation of its ordered meso-structure [55]. An attempt was made in this work to estimate the right amount of MPTMS/APTMS required to functionalise the support. Samples with increased organosilane amounts were synthesised and a MPTMS/APTMS: TEOS molar ratio equal to 2 was found to be the upper cut-off for an unchanged meso-structure. This finding was in good agreement with the literature, which stated that the meso-structures of APTES-functionalized SBA-15 materials prepared with a molar ratio of APTES:TEOS lower than 10 can be substantially conserved [56].

The samples were labelled as Au-0.6Mdp/SBA-15 and Au-0.6Adp/SBA-15, respectively. The fresh and spent Au-0.6Mdp/SBA-15 samples were characterised further along with the fresh Au-0.6Adp/SBA-15 sample.

### 3.2.3. Synthesis of Au-P/SBA-15 Catalyst (Impregnation)

In the current work, for the first time, a neutrally charged organo-phosphine ligand was synthesised and used to functionalise SBA-15 before gold loading. Phosphorus has previously been reported to form complexes with gold [57,58]. The idea was to investigate whether the attraction between phosphorus and gold could lead to the generation of very small gold particles on SBA-15.

SBA-15 was functionalised with 3-aminopropyltriethoxysilane, which basically yields Si-O$_3$Si-CH$_2$CH$_2$CH$_2$-NH$_2$. This was then reacted with Ph$_2$PCH$_2$OH. The P-CH$_2$OH groups are highly reactive towards amines, losing water to form a P-CH$_2$-N linkage, which is a neutral complex to form Si-O$_3$Si-CH$_2$CH$_2$CH$_2$-N (CH$_2$PPh$_2$)$_2$. To synthesise the catalyst, 1.0 g of functionalised support was suspended in 80 mL of distilled water and stirred for 30 min at 80 °C before adding 80 mg of HAuCl$_4$·3H$_2$O dissolved in 10 mL water. The solution colour gradually turned from light yellow to red within 7 min. The solution was cooled to room temperature for 20 min while stirring, and then recovered by filtration, air dried for 18 h, and then kept in an oven at 60 °C for 24 h. The sample was calcined to burn off the phosphine ligand in order to form gold nanoparticles on SBA-15. The catalyst was labelled as Au/P-SBA-15. Both fresh and spent samples were characterised.

### 3.3. Samples' Characterisation

The samples were characterised by TEM, XAFS, XPS, XRD, TPR, and CFR. The Au-0.6Mdp/SBA-15 sample, which proved to have the highest activity [50], was further characterised by the TAP Reactor. Transmission Electron Microscopy (TEM) images were obtained by using a JEOL 2100F FEG operating at 200 kV with samples ultrasonicated and dispersed onto holey carbon grids. Temperature Programmed Reduction and catalytic activity (TPR

and CFR)) experiments were performed in a CATLAB system (Hiden Analytical, UK). TPR was measured at heating rates of 10°/min, using a 30 mL/min flow rate of hydrogen (5% $H_2$ in argon balance). CFR measurements were carried out for a Gas Hourly Space Velocity (GHSV) of 45,000 $h^{-1}$ (20 mg of catalyst used). A flow of 40 mL/min of acetone mixed with a flow of 20 mL/min air from a gas cylinder (zero grade), making a total flow rate of 60 mL/min, were passed over the catalytic reactor. Acetone and $CO_2$ conversions were determined at three temperatures, i.e., 80, 180, and 280 °C. Wide angle X-Ray Diffraction spectroscopy (XRD) patterns were taken by using a Siemens D500 diffractometer with Cu $K_\alpha$ radiation (0.15406 nm), at a tube voltage of 40 kV and a 20 mA current with data collected over a 2θ range from 10° to 90°, with the scanning rate at 1°/min. XAFS (X-ray Absorption Fine Structure) measurements were performed at the Aichi SR facility (1.2 GeV 300 mA), BL 11 S2. The X-ray emitted from the super bending magnet was monochromatized by a Si (111) double crystal monochromator in transmission quick scan mode. Each sample was measured with 5 repetitions. The X-ray was monitored with three ionization chambers; the last one was for energy calibration using Au foil in between the second and the third ionization chamber. The ionization chambers were filled with $N_2$, $N_2$/Ar (75/25), and $N_2$/Ar (75/25) gases. REX2000 software was used to analyse the collected data [59]. The background was removed by spline smoothing with Cook-Sayers criterion [60]. The data were Fourier transformed over 3–16.9 $Å^{-1}$. The Fourier-transformed peak was inversely Fourier-transformed over 1.6–3.4 Å and curve fitting analyses were carried out in k-space using the empirical phase shift ($\phi(k)$) and backscattering amplitude ($F(k)$) derived from the Au foil measured at the same time (Equation (1)).

$$k^3 \chi\,(k) = k^3 \times \frac{NF(k)\exp\left(-2\sigma^2 k^2\right)}{kr^2}\,\sin(2kr + \phi(k)) \tag{4}$$

where *N*, *r* and *σ* are the coordination number, bond distance, and Debye-Waller factor, respectively, which are adjusted to obtain the best fit. *F(k)* and *φ(k)* are the backscattering amplitude and phase shift derived from Au foil.

X-ray photoelectron spectroscopy (XPS) measurements were performed on an JPC-9010MC (JEOL) X-ray photoelectron spectrometer with an Al K$\alpha$ X-ray radiation source (hν = 1486.6 eV). Binding energies were calibrated against the $Si2p_{3/2}$ peak energy of 103.6 eV for SBA-15.

TAP experiments were performed by using the TAP reactor system available at The University of Tokyo, which has been described in detail elsewhere [47,48]. Single-pulse, pump-probe, and multi-pulse experiments were completed using about 5 mg of catalyst, at temperatures from RT to 450 °C. The following ions were monitored: hydrogen ($m/z = 2$), acetone ($m/z = 42$), argon ($m/z = 39$), oxygen ($m/z = 31$), and $CO_2$ ($m/z = 43$).

The spent catalyst samples were those used in the acetone oxidation reaction for 25 h on stream at 270 °C.

## 4. Conclusions

For all samples, gold was present as metallic gold only. Depending on the preparation method, samples with gold nanoparticle's (cluster's) average size between 19 Å and 556 Å were obtained. The Au dispersion increased as the particle size decreased, i.e., 58% dispersion for the 19 Å particles, and only 2% dispersion for the 556 Å ones. As the dispersion increases, a contraction in the Au–Au bond distance occurs. The smaller the particle size, the higher the bond contraction. The maximum contraction was about 0.02 Å for the Au-0.6Mdp/SBA-15 fresh sample, for which the particle size was 19 Å. The Eley–Rideal mechanism, with a minor contribution from the Langmuir–Hinshelwood mechanism, was proposed for the acetone oxidation on Au/SBA-15 samples.

The samples showed high catalytic activity towards acetone oxidation. The catalytic activity depends on the particle size. The smaller the gold particle size, the higher the catalytic activity. The gold particle size can be controlled by modifying the preparation conditions leading to distinct interactions with the support.

To conclude, the novelty of the present paper refers to the following. To the best of our knowledge, this paper is the first to publish data on developed Au/SBA-15 catalysts tested for VOCs oxidation. Moreover, the temperature for the acetone complete conversion over the catalyst with the smallest particle size, observed at 250 °C, is the lowest among the gold/oxide catalysts' family. The TAP technique was used for the first time to study acetone removal, undoubtedly providing evidence of the reaction mechanism.

**Author Contributions:** Conceptualization, E.I., T.S., K.A. and M.O.; methodology, E.I. and M.O.; validation, E.I., H.A.-M., T.S., K.A. and M.O.; formal analysis, E.I., H.A.-M., T.S., K.A. and M.O.; investigation, E.I., H.A.-M., T.S., K.A. and M.O.; writing—original draft preparation, M.O.; writing— review and editing, E.I., H.A.-M., T.S., K.A. and M.O.; visualization, E.I., H.A.-M., T.S., K.A. and M.O. All authors have read and agreed to the published version of the manuscript.

**Conflicts of Interest:** The authors declare no conflict of interest.

## References

1. European Commission; Health & Consumer Protection Directorate-General. Directorate C—Public Health and Risk Assessment, C7—Risk assessment. In *Emission on Chemicals by Air Fresheners Tests on 74 Consumer Products Sold in Europe (BEUC Report January 2005)*; European Commission: Brussels, Belgium, 2005.
2. Eggert, T.; Hansen, O.C. Survey and emission of chemical substances from incense. *Surv. Chem. Subst. Consum. Prod.* **2004**, *39*, 1–136.
3. Manoukian, A.; Quivet, E.; Temime-Roussel, B.; Nicolas, M.; Maupetit, F.; Wortham, H. Emission characteristics of air pollutants from incense and candle burning in indoor atmospheres. *Environ. Sci. Pollut. Res.* **2012**, *20*, 4659–4670. [CrossRef] [PubMed]
4. Huang, H.; Xu, Y.; Feng, Q.; Leung, D.Y.C. Low temperaure catalytic oxidation of volatile organic compounds: A review. *Catal. Sci. Technol.* **2015**, *5*, 2649–2669. [CrossRef]
5. Kabir, E.; Kim, K.-H. A Review of Some Representative Techniques for Controlling the Indoor Volatile Organic Compounds. *Asian J. Atmospheric Environ.* **2012**, *6*, 137–146. [CrossRef]
6. Kamal, M.S.; Razzak, S.A.; Hossain, M.M. Catalytic oxidation of volatile organic compounds (VOCs)–A review. *Atmos. Environ.* **2016**, *140*, 117–134. [CrossRef]
7. Guo, Y.; Wen, M.; Li, G.; An, T. Recent advances in VOC elimination by catalytic oxidation technology onto various nano-particles catalysts: A critical review. *Appl. Catal. B Environ.* **2021**, *281*, 119447. [CrossRef]
8. Spivey, J.J. Complete catalytic oxidation of volatile organics. *Ind. Eng. Chem. Res.* **1987**, *26*, 2165–2180. [CrossRef]
9. Song, S.; Zhang, S.; Zhang, X.; Verma, P.; Wen, M. Advances in Catalytic Oxidation of Volatile Organic Compounds over Pd-Supported Catalysts: Recent Trends and Challenges. *Front. Mater.* **2020**, *7*, 119447. [CrossRef]
10. Gaálová, J.; Topka, P. Gold and Ceria as Catalysts for VOC Abatement: A Review. *Catalysts* **2021**, *11*, 789. [CrossRef]
11. Al-Aani, H.M.S.; Iro, E.; Chirra, P.; Fechete, I.; Badea, M.; Negrila, C.C.; Popescu, I.; Olea, M.; Marcu, I.-C. CuxCeMgAlO mixed oxide catalysts derived from multicationic LDH precursors for methane total oxidation. *Appl. Catal. A Gen.* **2019**, *586*, 117215. [CrossRef]
12. Liotta, L. Catalytic oxidation of volatile organic compounds on supported noble metals. *Appl. Catal. B Environ.* **2010**, *100*, 403–412. [CrossRef]
13. Pitkäaho, S.; Nevanperä, T.; Matejova, L.; Ojala, S.; Keiski, R.L. Oxidation of dichloromethane over Pt, Pd, Rh, and $V_2O_5$ catalysts supported on $Al_2O_3$, $Al_2O_3$–$TiO_2$ and $Al_2O_3$–$CeO_2$. *Appl. Catal. B Environ.* **2013**, *138–139*, 33–42. [CrossRef]
14. Haruta, M.; Kobayashi, T.; Sano, H.; Yamada, N. Novel Gold Catalysts for the Oxidation of Carbon Monoxide at a Temperature far Below 0 °C. *Chem. Lett.* **1987**, *16*, 405–408. [CrossRef]
15. Haruta, M. Size- and support-dependency in the catalysis of gold. *Catal. Today* **1997**, *36*, 153–166. [CrossRef]
16. Bond, G.C.; Thompson, D.T. Gold-catalysed oxidation of carbon monoxide. *Gold Bull.* **2000**, *33*, 41–50. [CrossRef]
17. Hashmi, A.S.K.; Hutchings, G.J. Gold catalysis, Angew. *Chem. Int. Ed. Engl.* **2006**, *45*, 7896–7936. [CrossRef] [PubMed]
18. Kiely, C.; He, Q.; Tiruvalam, R.; Herzing, A.; Hutchings, G. New Strategies for Controlling the Size, Morphology and Composition of Bimetallic and Trimetallic Catalyst Particles. *Microsc. Microanal.* **2013**, *19*, 1686–1687. [CrossRef]
19. Taketoshi, A.; Haruta, M. Size- and Structure-specificity in Catalysis by Gold Clusters. *Chem. Lett.* **2014**, *43*, 380–387. [CrossRef]
20. Akolekar, D.B.; Bhargava, S.K. Investigations on gold nanoparticles in mesoporous and microporous materials. *J. Mol. Catal. A Chem.* **2005**, *236*, 77–86. [CrossRef]
21. Bond, G. Source of the catalytic activity of gold nanoparticles. *Gold Bull.* **2010**, *43*, 88–93. [CrossRef]
22. Erenburg, S.; Trubina, S.; Bausk, N.; Moroz, B.; Kalinkin, A.; Bukhtiyarov, V.; Nikitenko, S. Structure of catalytically active gold nanopaticles by XAFS spectroscopy. *J. Phys. Conf. Ser.* **2009**, *190*, 012121. [CrossRef]
23. Grisel, R.; Weststrate, K.-J.; Gluhoi, A.; E Nieuwenhuys, B. Catalysis by Gold Nanoparticles. *Gold Bull.* **2002**, *35*, 39–45. [CrossRef]

24.  Zhao, D.; Huo, Q.; Feng, J.; Chmelka, B.F.; Stucky, G.D. Nonionic Triblock and Star Diblock Copolymer and Oligomeric Surfactant Syntheses of Highly Ordered, Hydrothermally Stable, Mesoporous Silica Structures. *J. Am. Chem. Soc.* **1998**, *120*, 6024–6036. [CrossRef]

25.  Zhao, D.; Feng, J.; Huo, Q.; Melosh, N.; Fredrickson, G.H.; Chmelka, B.F.; Stucky, G.D. Triblock Copolymer Syntheses of Mesoporous Silica with Periodic 50 to 300 Angstrom Pores. *Science* **1998**, *279*, 548–552. [CrossRef] [PubMed]

26.  Zhou, L.; Hu, J.; Xie, S.; Liu, H. Dispersion of Active Au Nanoparticles on Mesoporous SBA-15 Materials. *Chin. J. Chem. Eng.* **2007**, *15*, 507–511. [CrossRef]

27.  Odiba, S.; Olea, M.; Sasaki, T.; Iro, E.; Hodgson, S.; Adgar, A.; Russell, P. Micro-Reactor System for Complete Oxidation of Volatile Organic Compounds. *Catalysts* **2020**, *10*, 846. [CrossRef]

28.  Waters, R.D.; Weimer, J.J.; Smith, J.E. An investigation of the activity of coprecipitated gold catalysts for methane oxidation. *Catal. Lett.* **1995**, *30*, 181–188. [CrossRef]

29.  Haruta, M.; Ueda, A.; Tsubota, S.; Sanchez, R.T. Low-temperature catalytic combustion of methanol and its de-composed derivatives over supported gold catalysts. *Catal. Today* **1996**, *29*, 443–447. [CrossRef]

30.  Kim, H.S.; Kim, H.J.; Kim, J.H.; Kim, J.H.; Kang, S.H.; Ryu, J.H.; Park, N.-K.; Yun, D.-S.; Bae, J.-W. Noble-Metal-Based Cat-alytic Oxidation Technology Trends for Volatile Organic Compound (VOC) Removal. *Catalysts* **2022**, *12*, 63. [CrossRef]

31.  Mu, X.; Ding, H.; Pan, W.; Zhou, Q.; Du, W.; Qiu, K. Research progress in catalytic oxidation of volatile organic compound ace-tone. *J. Environ. Chem. Eng.* **2021**, *2*, 105650. [CrossRef]

32.  Minicò, S.; Scirè, S.; Crisafulli, C.; Galvagno, S. Influence of catalyst pretreatments on volatile organic compounds oxidation over gold/iron oxide. *Appl. Catal. B Environ.* **2001**, *34*, 277–285. [CrossRef]

33.  Scirè, S.; Riccobene, P.M.; Crisafulli, C. Ceria supported group IB metal catalysts for the combustion of volatile organic compounds and the preferential oxidation of CO. *Appl. Catal. B Environ.* **2010**, *101*, 109–117. [CrossRef]

34.  Carabineiro, S.; Chen, X.; Martynyuk, O.; Bogdanchikova, N.; Avalos-Borja, M.; Pestryakov, A.; Tavares, P.; Órfão, J.; Pereira, M.; Figueiredo, J. Gold supported on metal oxides for volatile organic compounds total oxidation. *Catal. Today* **2015**, *244*, 103–114. [CrossRef]

35.  Lu, Z.; Sham, T.; Norton, P. Interaction of Au on Si(100) studied by core level binding energy shifts. *Solid State Commun.* **1993**, *85*, 957–959. [CrossRef]

36.  Egelhoff, W. Core-level binding-energy shifts at surfaces and in solids. *Surf. Sci. Rep.* **1987**, *6*, 253–415. [CrossRef]

37.  Hansen, T.W.; DeLaRiva, A.T.; Challa, S.R.; Datye, A.K. Sintering of Catalytic Nanoparticles: Particle Migration or Ostwald Ripening? *Accounts Chem. Res.* **2013**, *46*, 1720–1730. [CrossRef]

38.  Leff, D.V.; Ohara, P.C.; Heath, J.R.; Gelbart, W.M. Thermodynamic Control of Gold Nanocrystal Size: Experiment and Theory. *J. Phys. Chem.* **1995**, *99*, 7036–7041. [CrossRef]

39.  Mori, T.; Hegmann, T. Determining the composition of gold nanoparticle: A compilation of shapes, sizes, and calculations using geometric considerations. *J. Nanopart. Res.* **2016**, *18*, 295. [CrossRef]

40.  Asakura, K.; Takakusagi, S.; Ariga, H.; Chun, W.-J.; Suzuki, S.; Koike, Y.; Uehara, H.; Miyazaki, K.; Iwasawa, Y. Preparation and structure of a single Au atom on the $TiO_2$(110) surface: Control of the Au–metal oxide surface interaction. *Faraday Discuss.* **2012**, *162*, 165–177. [CrossRef]

41.  Takakusagi, S.; Kunimoto, A.; Sirisit, N.; Uehara, H.; Ohba, T.; Uemuara, Y.; Wada, T.; Ariga, H.; Chun, W.-J.; Iwasawa, Y.; et al. A New Indicator for Single Metal Dispersion on a $TiO_2$(110) Surface Premodified with a Mercapto Compound. *J. Phys. Chem. C* **2016**, *120*, 15785–15791. [CrossRef]

42.  Miller, J.; Kropf, A.; Zha, Y.; Regalbuto, J.; Delannoy, L.; Louis, C.; Bus, E.; van Bokhoven, J. The effect of gold particle size on AuAu bond length and reactivity toward oxygen in supported catalysts. *J. Catal.* **2006**, *240*, 222–234. [CrossRef]

43.  Jain, P.K. A DFT-Based Study of the Low-Energy Electronic Structures and Properties of Small Gold Clusters. *Struct. Chem.* **2005**, *16*, 421–426. [CrossRef]

44.  Marinkovic, N.S.; Sasaki, K.; Adzic, R.R. Determination of Single- and Multi-Component Nanoparticle Sizes by X-ray Ab-sorption Spectroscopy. *J. Electrochem. Soc.* **2018**, *165*, J3222–J3230. [CrossRef]

45.  Yablonskii, G.S.; Shekhtman, S.O.; Chen, S.; Gleaves, J.T. Moment-Based Analysis of Transient Response Catalytic Studies (TAP Experiment). *Ind. Eng. Chem. Res.* **1998**, *37*, 2193–2202. [CrossRef]

46.  Gleaves, J.T.; Ebner, J.R.; Kuechler, T.C. Temporal Analysis of Products (TAP)—A Unique Catalyst Evaluation System with Submillisecond Time Resolution. *Catal. Rev.* **1988**, *30*, 49–116. [CrossRef]

47.  Olea, M.; Kunitake, M.; Shido, T.; Asakura, K.; Iwasawa, Y. Temporal Analysis of Products (TAP) Study of the Adsorption of CO, $O_2$, and $CO_2$ on a Au/Ti(OH)$_4$* Catalyst. *Bull. Chem. Soc. Jpn.* **2001**, *74*, 255–265. [CrossRef]

48.  Olea, M.; Kunitake, M.; Shido, T.; Iwasawa, Y. TAP study on CO oxidation on a highly active Au/Ti (OH)4* catalyst. *Phys. Chem. Chem. Phys.* **2001**, *3*, 627–631. [CrossRef]

49.  Yang, C.-M.; Kalwei, M.; Schüth, F.; Chao, K.-J. Gold nanoparticles in SBA-15 showing catalytic activity in CO oxidation. *Appl. Catal. A Gen.* **2003**, *254*, 289–296. [CrossRef]

50.  Iro, E. Synthesis of Stable Gold Nano-Particles on Optimised SBA-15 Support as an Effective Oxidation Catalyst for Low Temper-Ature Elimination of Volatile Organic Compounds. Ph.D. Thesis, Teesside University, Middlesbrough, UK, 2017.

51.  Avgouropoulos, G.; Oikonomopoulos, E.; Kanistras, D.; Ioannides, T. Complete oxidation of ethanol over alkali-promoted Pt/Al2O3 catalysts. *Appl. Catal. B Environ.* **2006**, *65*, 62–69. [CrossRef]

52. Gandía, L.; Vicente, M.; Gil, A. Complete oxidation of acetone over manganese oxide catalysts supported on alumina- and zirconia-pillared clays. *Appl. Catal. B Environ.* **2002**, *38*, 295–307. [CrossRef]

53. Block, B.; Bailar, J.J. The Reaction of Gold (III) with Some Bidentate Coordinating Groups-Correction. *J. Am. Chem. Soc.* **1951**, *75*, 6357. [CrossRef]

54. Zhu, H.; Liang, C.; Yan, W.; Overbury, S.H.; Dai, S. Preparation of highly active silica-supported Au catalysts for CO oxi-dation by a solution-based technique. *J. Phys. Chem. B* **2006**, *110*, 10842–10848. [CrossRef] [PubMed]

55. Hoffmann, F.; Cornelius, M.; Morell, J.; Fröba, M. Silica-Based Mesoporous Organic–Inorganic Hybrid Materials. *Angew. Chem. Int. Ed.* **2006**, *45*, 3216–3251. [CrossRef]

56. Chong, A.S.M.; Zhao, X.S. Functionalization of SBA-15 with APTES and Characterization of Functionalized Materials. *J. Phys. Chem. B* **2003**, *107*, 12650–12657. [CrossRef]

57. McAuliffe, C.A.; Parish, R.V.; Randall, D.P. Gold(I) complexes of unidentate and bidentate phosphorus-, arsenic-, antimony-, and sulphur-donor ligands. *J. Chem. Soc. Dalton Trans.* **1979**, *11*, 1730–1735. [CrossRef]

58. Slany, M.; Bardaji, M.; Casanove, M.-J.; Caminade, A.-M.; Majoral, J.-P.; Chaudret, B. Dendrimer Surface Chemistry. Facile Route to Polyphosphines and Their Gold Complexes. *J. Am. Chem. Soc.* **1995**, *117*, 9764–9765. [CrossRef]

59. Iwasawa, Y. *X-ray Absorption Fine Structure for Catalysts and Surface*; World Scientific: Singapore, 1996; pp. 35–58.

60. Cook, J.W., Jr.; Sayers, D.E. Criteria for automatic x-ray absorption fine structure background removal. *J. Appl. Phys.* **1981**, *52*, 5024–5031. [CrossRef]